

# Titania Nanosheets Generates Peroxynitrite for S-Nitrosylation and Enhanced p53 Function in Lung Cancer Cells

**Rapeepun Soonnarong**

Chulalongkorn University

**Sucharat Tungsukruthai**

Chulalongkorn University

**Bodee Nutho**

Mahidol University Faculty of Science

**Thanyada Rungrotmongkol**

Chulalongkorn University Faculty of Science

**Chanida Vinayanuwattikun**

Chulalongkorn University Faculty of Medicine

**Tosapol Maluangnont**

King Mongkut's Institute of Technology Ladkrabang

**pithi chanvorachote** (✉ [pithi.ch@gmail.com](mailto:pithi.ch@gmail.com))

Chulalongkorn University Faculty of Pharmaceutical Sciences <https://orcid.org/0000-0002-3103-3249>

---

## Research

**Keywords:** Apoptosis, Nanosheets, Lung cancer, p53, S-nitrosylation, Peroxynitrite, Molecular dynamics

**Posted Date:** June 15th, 2021

**DOI:** <https://doi.org/10.21203/rs.3.rs-607927/v1>

**License:**   This work is licensed under a Creative Commons Attribution 4.0 International License.

[Read Full License](#)

---

## RESEARCH

# Titania Nanosheets Generates Peroxynitrite for S-Nitrosylation and Enhanced p53 Function in Lung Cancer Cells

Rapeepun Soonnarong<sup>1,2</sup>, Sucharat Tungsukruthai<sup>1,2</sup>, Bodee Nutho<sup>4</sup>, Thanyada Rungrotmongkol<sup>5,6</sup>, Chanida Vinayanuwattikun<sup>7</sup>, Tosapol Maluangnont<sup>8</sup> and Pithi Chanvorachote<sup>2,3\*</sup>

\*Correspondence:

pithi\_chan@yahoo.com

<sup>2</sup>Departments of Pharmacology and Physiology, Faculty of Pharmaceutical Sciences, Bangkok, 10330, Thailand

Full list of author information is available at the end of the article

## Abstract

**Background:** Metal oxide nanomaterials are increasingly being exploited in cancer therapy thanks to their unique properties, which can enhance the efficacy of current cancer therapies. However, the nanotoxicity and mechanism of  $Ti_{0.8}O_2$  nanosheets for specific site-targeting strategies in NSCLC have not yet been investigated.

**Methods:** The effects of  $Ti_{0.8}O_2$  nanosheets on cytotoxicity in NSCLC cells and normal cells were examined. The apoptosis characteristics, including condensed and fragmented nuclei, as assessed by positive staining with annexin V. The cellular uptake of the nanosheets and the induction of stress fiber were assessed via transmission electron microscopy (TEM) and scanning electron microscopy (SEM) analyses, respectively. We also evaluated the expression of protein in death mechanism to identify the molecular mechanisms behind the toxicity of these cells. We investigated the relationship between S-nitrosylation and the increase in p53 stability by molecular dynamics.

**Results:**  $Ti_{0.8}O_2$  nanosheets caused cytotoxicity in several lung cancer cells, but not in normal cells. The nanosheets could enter lung cancer cells and exert an apoptosis induction. Results for protein analysis further indicated the activation of p53, increased Bax, decreased Bcl-2 and Mcl-1, and activation of caspase-3. The nanosheets also exhibited a substantial apoptosis effect in drug-resistant metastatic primary lung cancer cells, and it was found that the potency of the nanosheets was dramatically higher than that of cisplatin and etoposide. In terms of their mechanism of action, we found that the mode of apoptosis induction was through the generation of cellular  $ONOO^-$  mediated the S-nitrosylation of p53 at C182. Molecular dynamics analysis further showed that the S-nitrosylation of one C182 stabilized the p53 dimer. Consequently, this nitrosylation of the protein led to an upregulation of p53 through its stabilization.

**Conclusions:** Taking all the evidence together, we provided information on the apoptosis induction effect of the nanosheets through a molecular mechanism involving reactive nitrogen species, which affects the protein stability; thus emphasizing the novel mechanism of action of nanomaterials for cancer therapy.

**Keywords:** Apoptosis, Nanosheets, Lung cancer, p53, S-nitrosylation, Peroxynitrite, Molecular dynamics

## Background

Lung cancer is one of the most common cancers worldwide and has the highest mortality rate. Although a number of crucial components in the fight against lung cancer have been elucidated, including small molecule tyrosine kinase inhibitors, and immunotherapy developed, which have led to unprecedented survival benefits in selected patients, the overall cure and survival rates for non-small cell lung cancer (NSCLC) remain low [1]. Therefore, continued research into new drugs and combination therapies is required to expand the clinical benefit to a broader patient population and to improve the outcomes in NSCLC. The tumor suppressor p53 is an essential regulatory molecule that is implicated in cell cycle arrest and plays a mediator role in apoptosis in response to stress [2]. A key attribute of the p53 response is p53 stabilization, which results in a rapid increase in p53 steady-state levels. Considerable evidence has indicated that p53 stabilization largely depends on post-translational events that disengage p53 from its proteasomal degradation [3]. In all cases, this includes a series of post-translational modifications, some of which are known to impact the interaction between p53 and the mouse double minute 2 (MDM2) protein, representing the major mechanism for controlling p53 stability [4]. The activation of p53 results in an increase in BH3-only proteins promoting Bax/Bak oligomerization. The induction of pro-apoptotic signaling leads to the formation of mitochondrial pores, the release of cytochrome c into the cytosol, the activation of caspases, and finally cell apoptosis [5]. In contrast, the dysregulation of apoptosis in lung cancer can be caused by several mechanisms; however, upregulation of the expression of pro-survival proteins, including mammalian target of rapamycin (mTOR), and anti-apoptotic proteins of the Bcl-2 family, has been shown to be the predominant mechanism [6].

p53, an important tumor suppressor protein, has been intensively investigated as its functions are critical for cancers. The functions of the p53 protein are tightly associated with its protein conformation. The active conformation of this protein is the tetrameric form via an interaction of the tetramerization domain (TD) on the p53 protein. Studies have pointed out that the tetramerization of p53 is critical for DNA binding, and post-translational modification, as well as for p53 stability [7]. Cysteine thiol groups on the p53 molecule have been highlighted as sensitive sites for protein modification, and it was shown that the DNA-binding affinity could be altered by thiol blocking agents [8]. Certain cysteine residue amino acid replacements inhibit the binding of p53 to DNA [9]. In addition, several lines of evidence have demonstrated that the oxidative modification of cysteine residues within p53 can also influence the protein's activity and stability [10-12].

Nitric oxide (NO) is a key intercellular messenger synthesized from l-arginine in a reaction catalyzed by NO synthases (NOS). Nitric oxide is recognized as an important signaling device for controlling practically all critical cellular functions, and it is also a strong mediator of cellular damage [13]. Nitric oxide plays an extensive role in regulating the expression of eukaryotic genes, and this effect is exerted in part through S-nitrosylation [14]. S-Nitrosylation of the controlling binding associates of the transcription factors can exert an extranuclear effect on transcription factor activation, stability, and/or nuclear targeting, as in the case of hypoxia-inducible factor-1 $\alpha$  (HIF-1 $\alpha$ ) and p53 [15]. In addition, nitric oxide can react with superoxide (O<sub>2</sub><sup>•-</sup>) to form the much more powerful oxidant peroxynitrite (ONOO<sup>-</sup>), which is a key component determining the contrasting roles of nitric oxide in physiology and pathology [16]. Many of the biological effects ascribed with nitric oxide are actually related to the intermediate peroxynitrite. Even though peroxynitrite is a powerful oxidant, it reacts at a moderately slow rate with most biological molecules and is able to reach cell membranes in part through anion channels [17]. This makes the biological and pathological insinuations of peroxynitrite much more interesting, because it can have more delicate and specific actions on cells.

Nanotechnology is a research field that has wide implications in the fields of chemistry, engineering, biology, and medicine. Nanotechnology has several applications in cancer biology, especially in the development of novel treatments [18].

44

45

46

47

48

49

50

51

52

53

54

55

56

57

58

59

60

61

62

63

64

65

66

67

68

69

70

71

72

73

74

75

76

77

78

79

80

81

82

83

84

85

86

87

88

89

90

91

92

93

94

95

96

97

98

99

100

101 Nanosheets are a developing class of nanomaterial that are highly anisotropic and  
102 flexible [19]. Moreover,  $\text{Ti}_{0.8}\text{O}_2$  nanosheets have also been found to induce superoxide  
103 anions in cancer without harming normal dermal papilla cells [20]. However, to the  
104 best of our knowledge, the nanotoxicity and mechanism of  $\text{Ti}_{0.8}\text{O}_2$  nanosheets for  
105 specific site-targeting strategies in NSCLC have not yet been investigated.  
106 Consequently, this study aimed to investigate the effects of  $\text{Ti}_{0.8}\text{O}_2$  nanosheets on the  
107 cytotoxicity of human non-small cell lung cancer (NSCLC) cells and to identify the  
108 molecular mechanisms behind the toxicity of these cells, which we reveal to be related  
109 to ROS generation-mediated apoptosis via the mitochondrial pathway. This study  
110 could be valuable in the development of nanomaterials for anticancer approaches.  
111

## 112 Results

### 113 Synthesis and characterization of the $\text{Ti}_{0.8}\text{O}_2$ nanosheets

114 The preparation of the  $\text{Ti}_{0.8}\text{O}_2$  nanosheets from the lepidocrocite-type  $\text{K}_{0.8}\text{Zn}_{0.4}\text{Ti}_{1.6}\text{O}_4$   
115 is shown schematically in Figure 1A. Here, the  $\text{K}^+$  ion (0.8 per the formula unit)  
116 alternately stacks with the negatively-charged sheets of edge-shared  $(\text{Ti,Zn})\text{O}_6$   
117 octahedra (i.e., the  $\text{Zn}_{0.4}\text{Ti}_{1.6}\text{O}_4^{0.8-}$  sheet with  $\sim 1$  nm thickness). Reacting the solid with  
118 1 M HCl led to a quantitative replacement of  $\text{K}^+$  with  $\text{H}_3\text{O}^+$  and an almost complete Zn  
119 leaching. The subsequent reaction of the solid with the bulky  $\text{TBA}^+$  ions resulted in the  
120 infinite separation of stacks of sheets into individual nanosheets.

121 As shown in Figure 1B, the obtained colloidal suspension was white and with a  
122 blue tint. It absorbed light at  $\lambda_{\text{max}} = 261$  nm, which is consistent with previous  
123 reports. A clear Tyndall effect could be observed where laser illumination was  
124 scattered throughout, suggesting the presence of nanosheets. The Dynamic Light  
125 Scattering provided the size estimation of the  $\text{Ti}_{0.8}\text{O}_2$  nanosheets as  $\sim 268$  nm, see  
126 Figure 1C. The zeta potential of  $-30$  mV agreed well with their negatively-charged  
127 nature. Figure 1D is a representative TEM image, showing several uniform-contrast,  
128 flat objects (i.e., nanosheets) with lateral dimensions of up to  $\sim 200$  nm. Altogether,  
129 the different characterization techniques confirmed the successful preparation of the  
130 negatively-charged  $\text{Ti}_{0.8}\text{O}_2^{0.8-}$  nanosheets (or simply  $\text{Ti}_{0.8}\text{O}_2$  nanosheets) in contrast to  
131 typically  $\text{TiO}_2$  with is charge-neutral. Detail characterizations can be found elsewhere  
132 (Mol Pharm 95 2019 418; ACS Appl Mater Interfaces 2 2019 3840).  
133

### 134 Cytotoxicity of the $\text{Ti}_{0.8}\text{O}_2$ nanosheets on human lung cancer cells and normal cells

135 Cells were treated with various concentrations of  $\text{Ti}_{0.8}\text{O}_2$  nanosheets (0–100  $\mu\text{g}/\text{mL}$ )  
136 and analyzed by MTT assay. The results revealed the statistically significant cytotoxic  
137 effects of  $\text{Ti}_{0.8}\text{O}_2$  nanosheets occurred at concentrations of 10–100  $\mu\text{g}/\text{mL}$  in A549,  
138 H460, and H23 cells and at 20–100  $\mu\text{g}/\text{mL}$  in H292 cells. In the primary dermal papilla  
139 cells from different sources (DP1 and DP2), cytotoxic effects of the  $\text{Ti}_{0.8}\text{O}_2$  nanosheets  
140 were found at 50  $\mu\text{g}/\text{mL}$ . Moreover, at the concentration of 30  $\mu\text{g}/\text{mL}$ , the  $\text{Ti}_{0.8}\text{O}_2$   
141 nanosheets showed statistically significant cytotoxic effects on DP and HaCat cells  
142 (Fig. 2A–H). Characteristic apoptosis cells were identified using a nuclear staining  
143 assay. The results showed that the  $\text{Ti}_{0.8}\text{O}_2$  nanosheets mediated apoptosis in lung  
144 cancer cells at concentrations of 1–10  $\mu\text{g}/\text{m}$ , with a small percentage of necrotic cells  
145 (Fig. 2I–L). Flow cytometry analysis based on annexin V/PI detection also confirmed  
146 that 10  $\mu\text{g}/\text{mL}$  of  $\text{Ti}_{0.8}\text{O}_2$  nanosheets induced dramatic apoptosis in A549 and H460  
147 cells when compared with untreated cells (Fig. 2M–N).  
148

### 149 Uptake of the $\text{Ti}_{0.8}\text{O}_2$ nanosheets by cancer cells

150 Under SEM morphological analysis, it was seen that for H460 cells, the morphology of  
151 the cancer cells gradually changed, including the formation of stress fibers, when  
152 treated with  $\text{Ti}_{0.8}\text{O}_2$  nanosheets at concentrations of 1–10  $\mu\text{g}/\text{mL}$  (Fig. 3A). Moreover,  
153 TEM analysis showed that  $\text{Ti}_{0.8}\text{O}_2$  nanosheets at 10  $\mu\text{g}/\text{mL}$  could appropriately pass  
154 into the H460 cells (Fig. 3B).  
155

### 156 $\text{Ti}_{0.8}\text{O}_2$ nanosheets modulate apoptosis-related proteins in H460 and A549 cells

157 In order to investigate the mechanism of  $\text{Ti}_{0.8}\text{O}_2$  nanosheets-induced apoptosis, the  
158 apoptotic-related proteins were determined by Western blot analysis. A549 and H460  
159 cells were treated with 0–10  $\mu\text{g}/\text{mL}$   $\text{Ti}_{0.8}\text{O}_2$  nanosheets, and then the pro- and anti-

apoptotic proteins related to mitochondria-mediated apoptosis were evaluated. The results showed that the  $\text{Ti}_{0.8}\text{O}_2$  nanosheets increased the pro-apoptotic protein Bax, whereas the anti-apoptotic proteins Mcl-1 and Bcl-2 were downregulated in the cells treated with the  $\text{Ti}_{0.8}\text{O}_2$  nanosheets. In addition, pro-caspase3 was decreased in a concentration-dependent manner. Moreover, p53 was found to be activated in response to the treatment with the  $\text{Ti}_{0.8}\text{O}_2$  nanosheets (Fig. 3C and D). Taken together, it can be concluded that the  $\text{Ti}_{0.8}\text{O}_2$  nanosheets mediated the apoptosis of lung cancer cells by increasing the pro-apoptotic proteins, which led to cell death by the mitochondria-dependent pathway.

#### **Cytotoxicity and apoptotic effects of $\text{Ti}_{0.8}\text{O}_2$ nanosheets on advanced lung cancer cells from patients**

To assess the potential pharmacological activities of synthetic  $\text{Ti}_{0.8}\text{O}_2$  nanosheets compounds in advanced lung cancer cells, treatment with the current standard therapeutic agents was also performed for comparison. Two groups of cell lines were used for the investigations: panel A, an advanced non-small cell lung cancer cell line from patients with malignant pleural effusion who had never been treated by chemotherapy, targeted therapy, or immunotherapy; and panel B, an advanced non-small cell lung cancer cell line from patients with malignant pleural effusion who had been treated with standard platinum-doublet chemoRx with or without targeted therapy or a checkpoint inhibitor and second-line chemoRx. In total, six primary lung cancer cells were treated with the same concentrations of  $\text{Ti}_{0.8}\text{O}_2$  nanosheets, cisplatin, and etoposide (0–100  $\mu\text{g}/\text{mL}$ ) for 24 hours and subjected to cell viability analysis by MTT assay. The  $\text{Ti}_{0.8}\text{O}_2$  nanosheets could be considered nontoxic at doses lower than 1  $\mu\text{g}/\text{mL}$ , while a concentration of more than 10  $\mu\text{g}/\text{mL}$  caused a significant decrease in the cell viability of the cells (Fig. 4A–F); whereas, the standard drugs showed a slightly decreased cell viability from 0.5  $\mu\text{g}/\text{mL}$  to 100  $\mu\text{g}/\text{mL}$ , while doses of more than 20  $\mu\text{g}/\text{mL}$  cisplatin and etoposide were considered toxic. Data analysis showed that the  $\text{IC}_{50}$  of the  $\text{Ti}_{0.8}\text{O}_2$  nanosheets was lower than 10  $\mu\text{g}/\text{mL}$  at 24 h, which was significantly lower than for cisplatin and etoposide (Fig. 4M and N). The results showed that the  $\text{Ti}_{0.8}\text{O}_2$  nanosheets reduced cell viability in a concentration-dependent manner compared with the untreated controls (Fig. 4A–F). To confirm the effect of the  $\text{Ti}_{0.8}\text{O}_2$  nanosheets on advanced lung cancer cells from patients, a nuclear staining assay using Hoechst 33342 and propidium iodide was performed and the results analyzed. After treatment with the compounds at 10  $\mu\text{g}/\text{mL}$  of  $\text{Ti}_{0.8}\text{O}_2$  nanosheets, apoptotic cells were observed by the presence of a nuclear condensation morphology in the representative cell line (Fig. 4H–M). The percentage cell viability was determined using the MTT assay to determine the  $\text{IC}_{50}$  values (Fig. 4G).

#### **Effect of $\text{Ti}_{0.8}\text{O}_2$ nanosheets on intracellular ROS induction in A549 and H460 cells**

Current developments in cancer research suggest that the generation of ROS through oxidative stress is a common mechanistic pathway of a number of apoptotic stimuli. ROS is considered an essential signaling molecule for the initiation and execution of apoptosis [32]. Consequently, we next investigated whether intracellular ROS generation was implicated in the anticancer effects of the  $\text{Ti}_{0.8}\text{O}_2$  nanosheets. The intracellular ROS level was evaluated using the fluorescent probe DCFH-DA. The results showed that treatment with  $\text{Ti}_{0.8}\text{O}_2$  nanosheets increased the intracellular ROS generation (Fig. 5A and B). In order to investigate the protective effect of N-acetylcysteine (NAC) or glutathione (GSH) as a potent antioxidant on  $\text{Ti}_{0.8}\text{O}_2$  nanosheets-induced cytotoxicity mediated through ROS generation, H460 and A549 cell lines were pretreated with NAC or GSH for 1 h previous to treatment with the  $\text{Ti}_{0.8}\text{O}_2$  nanosheets. We detected a decrease in the ROS level in all the cell lines treated with NAC and GSH (Fig. 5A and B), but the cell viability of the cancer cells could not be reversed by the pretreatment with NAC or GSH (Fig. 5C and D). These results suggested that the  $\text{Ti}_{0.8}\text{O}_2$  nanosheets induce cytotoxicity in cancer cell lines but did not do this via the generation of ROS. Next, we investigated the specific ROS products using a DHE (dihydroethidium) fluorescent probe for the detection of ROS generation, and specifically for the detection of superoxide anions. The results showed that the  $\text{Ti}_{0.8}\text{O}_2$  nanosheets had a significant effect on the superoxide anions in H460 cells

when they were treated with  $\text{Ti}_{0.8}\text{O}_2$  nanosheets in a concentration-dependent manner (Fig. 5E); while the  $\text{Ti}_{0.8}\text{O}_2$  nanosheets had only a slight effect on superoxide anion generation in A549 cells (Fig. 5E). In addition, we also investigated the generation of hydroxyl radicals using the HPF (hydroxyphenyl fluorescein) fluorescent probe in both cell lines. The results showed that the  $\text{Ti}_{0.8}\text{O}_2$  nanosheets significantly generated hydroxyl radicals in both cell lines compared with the non-treated cells (Fig. 5F). According to our obtained data, the pretreatment of cancer cell lines with a potent antioxidant for 1 h could not inhibit  $\text{H}_2\text{O}_2$  damage, while the  $\text{Ti}_{0.8}\text{O}_2$  nanosheets generated superoxide anion hydroxyl radicals in both cell lines.

#### **$\text{Ti}_{0.8}\text{O}_2$ nanosheets-mediated peroxynitrite induces apoptosis in A549 and H460 cells**

Nitric oxide plays a role in apoptosis regulation through its ability to modulate ROS. The cytotoxic capacity of nitric oxide has been confirmed in numerous systems using diverse cell targets. In many circumstances, the cytotoxicity is the result of the interaction of nitric oxide with superoxide to form peroxynitrite ( $\text{ONOO}^-$ ), a potent oxidant that is a key element in inducing cell death [33]. Consequently, we analyzed the cellular nitric oxide levels in response to the  $\text{Ti}_{0.8}\text{O}_2$  nanosheets using DAF-FM DA as a fluorescent probe. The nitric oxide levels were found to be increased in a concentration-dependent manner (Fig. 6A and C). Additionally, co-treatment with PTIO (a nitric oxide scavenger) and/or MnTBAP (a superoxide anion inhibitor) inhibited  $\text{Ti}_{0.8}\text{O}_2$  nanosheets -induced cell death by increasing cell viability (Fig. 6B and D). The results suggested that  $\text{Ti}_{0.8}\text{O}_2$  nanosheets induce cytotoxicity in cancer cell lines via the produced peroxynitrite. To confirm the previous results, we treated cells with  $\text{Ti}_{0.8}\text{O}_2$  nanosheets and/or pretreated them with PTIO and/or MnTBAP and then determined the cellular nitric oxide level by staining with DAF-FM DA and then visualizing under a fluorescence microscope. The results showed that the co-treatment with these inhibitors decreased peroxynitrite levels in all the cancer cells (Fig. 6F). Then, we observed whether increased peroxynitrite was required for cell apoptosis induced by  $\text{Ti}_{0.8}\text{O}_2$  nanosheets. The results showed that the co-treatment with these inhibitors was able to inhibit apoptosis cell death, as shown in Figure 6E. Collectively, these results indicated that peroxynitrite generation could play a role in mediating  $\text{Ti}_{0.8}\text{O}_2$  nanosheets -induced cell apoptosis.

#### **$\text{Ti}_{0.8}\text{O}_2$ nanosheets-mediated peroxynitrite induces apoptosis in A549 and H460 cells via p53 upregulation**

Since then, several cell types have been shown to undergo apoptosis in response to nitric oxide or peroxynitrite. A previous study reported that peroxynitrite was associated with p53 regulation to induce cancer cell death [33]. Therefore, we examined the effect of  $\text{Ti}_{0.8}\text{O}_2$  nanosheets when combined with PTIO and/or MnTBAP. Western blot analysis was performed to evaluate the p53 protein levels after 10  $\mu\text{g}/\text{ml}$   $\text{Ti}_{0.8}\text{O}_2$  nanosheets treatment in all the cell lines. The results showed that the p53 protein levels in all the cell lines were significantly increased with the  $\text{Ti}_{0.8}\text{O}_2$  nanosheets alone treatment compared with those of the non-treatment control and another condition treatment (Fig. 7A–C). Taking this together, it could be concluded that the  $\text{Ti}_{0.8}\text{O}_2$  nanosheets induced cancer cell death by the induction of peroxynitrite generation, which activated p53, leading to cancer cell apoptosis. The immunofluorescence staining results supported our finding that  $\text{Ti}_{0.8}\text{O}_2$  nanosheets in combination with PTIO and MnTBAP caused a dramatic decrease in the level of p53 and P-p53 in both cell lines (Fig. 7D and E). These results indicate that the pro-apoptotic effect of  $\text{Ti}_{0.8}\text{O}_2$  nanosheets for inducing nitric oxide was a result of the formation of peroxynitrite, which then induced p53-dependent apoptosis in all the cell lines.

#### **$\text{Ti}_{0.8}\text{O}_2$ nanosheets increase p53 function but not through p53 proteasomal degradation**

In healthy cells, p53 plays a pivotal role in responding to oncogenic stress signals and helps to keep cells metabolically stable [34]. The importance of p53 is highlighted by the fact that it is frequently altered in human cancers [35], [36]; indeed, even tumors that retain wild-type p53 are often compromised in their ability to activate the p53 pathway. The acute activation of p53 leads to numerous responses that prevent

278 further cell division, including cell cycle arrest, senescence, and apoptosis. In this way,  
279 p53 can prevent the outgrowth of incipient cancer cells. A protein abundance reflects  
280 the balance of the rates of protein synthesis and protein degradation. Key to the  
281 regulation of p53 is control of the stability of the p53 protein, which is mainly  
282 arranged through a network of ubiquitination reactions. We further evaluated the  
283 effect of the Ti<sub>0.8</sub>O<sub>2</sub> nanosheets on the Ti<sub>0.8</sub>O<sub>2</sub> nanosheets stability in lung cancer cells.  
284 To compare the Ti<sub>0.8</sub>O<sub>2</sub> nanosheets stability between Ti<sub>0.8</sub>O<sub>2</sub> nanosheets -treated cells  
285 and the control cells, the cycloheximide (CHX) chasing assay was used followed by  
286 Western blot analysis. CHX, an inhibitor of protein biosynthesis, is widely used for  
287 determining the half-life of proteins of interest [37]. Therefore, H460 and A549 cells  
288 were treated with Ti<sub>0.8</sub>O<sub>2</sub> nanosheets (10 µg/ml) in the presence or absence of 50  
289 µg/mL CHX, and the level of p53 over time was determined. Figures 8A, B show that in  
290 the condition where protein production was blocked, the Ti<sub>0.8</sub>O<sub>2</sub> nanosheets increased  
291 the stability of the p53 protein. A difference was first detected at 90 min after Ti<sub>0.8</sub>O<sub>2</sub>  
292 nanosheets treatment (Fig. 8A and B). We also determined the p53 protein half-life  
293 and found that the half-life of the p53 protein in the Ti<sub>0.8</sub>O<sub>2</sub> nanosheets -treated  
294 groups was about 60 min; whereas in the untreated control, the value was about 30–  
295 40 min (Fig. 8C).

296 Ubiquitin–proteasome degradation has been shown to influence protein turnover.  
297 Thus, MG132, a potent proteasome inhibitor, was used to prove that this increase in  
298 p53 stability was through proteasomal degradation of the protein by the Ti<sub>0.8</sub>O<sub>2</sub>  
299 nanosheets. We also checked the premise of ubiquitin-mediated p53 degradation  
300 using co-immunoprecipitation and evaluated the level of the p53-ubiquitin complex  
301 (poly Ub-p53) in H460 and A549 cells after treatment with 10 µg/ml of Ti<sub>0.8</sub>O<sub>2</sub>  
302 nanosheets and in non-treated control cells for 1 h. Figures 8D–E show that the  
303 polyubiquitination of p53 was noticeably diminished after Ti<sub>0.8</sub>O<sub>2</sub> nanosheets  
304 treatment when compared with the non-treated control; thus confirming that the  
305 Ti<sub>0.8</sub>O<sub>2</sub> nanosheets-mediated p53 stability did not occur through ubiquitin–  
306 proteasome degradation.  
307

### 308 **S-nitrosylation in the regulation of stability of the tetrameric p53 protein-protein** 309 **complex**

310 It has become increasingly evident that nitric oxide exerts its effects, in part, by the S-  
311 nitrosylation of cysteine (Cys) residues. The S-nitrosylation of a single Cys within  
312 HDM2 inhibits p53 binding and thereby stabilizes p53 and activates p53-dependent  
313 transcription [38]. We tested *in vitro* whether peroxynitrite may directly control p53  
314 by S-nitrosylation and the activation of p53. Sulfhydryl sensitivity and reversibility are  
315 consistent with nitrosylation. Finally, we identified a critical cysteine residue that  
316 nitric oxide modifies to disrupt p53 binding. To evaluate the structural stability of the  
317 p53 core domain tetramer (Fig. 9A), the number of intermolecular hydrogen bonds  
318 formed between each monomer at the protein–protein interface was monitored along  
319 with the simulation time. Note that a hydrogen bond was defined by the following  
320 geometric criteria: (i) the distance between the hydrogen bond donor (D) and  
321 acceptor (A) atoms is less than 3.5 Å, and (ii) the angle between D–H•••A is greater  
322 than 120°. The obtained results showed that there was an average of  $\sim 10 \pm 2$   
323 hydrogen bonds steadily formed over the course of the simulation time (Fig. 9B, top).  
324 This observation suggested that our simulation model was highly stable. Therefore,  
325 the equilibrated 100 MD snapshots extracted from the last 20 ns were used for further  
326 analysis in terms of the  $\Delta G_{\text{bind}}^{\text{residue}}$  calculation.

327 The  $\Delta G_{\text{bind}}^{\text{residue}}$  was then calculated to verify the crucial amino acids involved in  
328 protein binding at the interface region of each monomer. The total contributing  
329 energy from each amino acid for the protein–protein complex is shown in Figure 9C  
330 (top), where the positive and negative  $\Delta G_{\text{bind}}^{\text{residue}}$  values are associated with protein  
331 destabilization and stabilization, respectively. It is noteworthy that only amino acids  
332 exhibiting a  $\Delta G_{\text{bind}}^{\text{residue}}$  of  $< -1.5$  kcal/mol were marked as the key binding residues. The  
333 results showed that the crucial residues (L93, N167, M169, C176, P177, and E180 for  
334 monomer A; H178, E180, R181, N200, L201, and V225 for monomer B; C176, P177,  
335 H178, E180, R181, E198, L201, E224, V225, and H233 for monomer C; V97, N100,

N167, M169, C176, P177, E180, and R181 for monomer D) played a pivotal role in the tetrameric protein–protein stabilization. Based on this calculation and upon visual inspection, it can be assumed that the cysteine residue within the protein–protein interface, particularly C182, was most likely to be a critical residue, which would be expected to be related to the *S*-nitrosylation site and consequently would lead to an increase in protein stability. To clarify such an hypothesis, the influence of *S*-nitrosylation at the C182 residue of p53 on its binding interaction with each monomeric p53 was investigated by means of MD simulation, as per the native p53 system. The simulation indicated that the total number of intermolecular hydrogen bonds between four monomeric proteins was slightly increased over the whole simulation, with an average value of  $\sim 12 \pm 2$  hydrogen bonds, particularly in the last 10 ns (90–100 ns), in which the number of hydrogen bonds was found to be up to  $\sim 20$  (Fig. 9B, bottom). This reflected that the *S*-nitrosylated C182 resulted in a higher stability of the tetrameric protein–protein complex compared to the native p53. In addition, the occurrence of the C182 *S*-nitrosylation appeared to induce the surrounding residues located in the interface region to bind more tightly to each other, especially the residues 176–186 (Fig. 9C, bottom and Fig. 9D). Among these amino acids, the lowest  $\Delta G_{\text{bind}}^{\text{residue}}$  value ( $\sim -5$  to  $-7$  kcal/mol) was observed for residue R181, most likely owing to the indirect stabilizing effect of the *S*-nitrosylation at C182. This was probably one of the reasons why the *S*-nitrosylation culminated in a higher stability of p53, as observed in the experimental data.

## Discussion

Lung cancer remains the major cause of cancer death worldwide. Nowadays, nanomaterials are showing remarkable potential to aid the diagnosis and treatment of cancer by enabling the more effective targeting of tumors [39]. Previous studies have revealed that nanomaterials can selectively sink in solid tumors, whereby they increase the bioavailability and decrease the toxicity of the encapsulated cytotoxic agents [39,40].  $\text{Ti}_{0.8}\text{O}_2$ , an emerging 2D analog of  $\text{TiO}_2$ , nanosheets can be derived from the potassium zinc titanate precursor  $\text{K}_{0.8}\text{Zn}_{0.4}\text{Ti}_{1.6}\text{O}_4$ . The planar surface and functional motifs of such 2D inorganic nanosheets can be modified using a surface engineering process via chemical bonding or physical adsorption [22], which favors subsequent nanomedical applications in specific physiological environments, through e.g., their biostability improvement, site-specific targeting capability, and multiple theranostic functions to facilitate oncological applications [18,40,41].

Although nanoparticles and nanotubes of  $\text{TiO}_2$  have been extensively studied regarding biomedical applications [41,42], to the best of our knowledge, there are no studies on  $\text{Ti}_{0.8}\text{O}_2$  nanosheets. Consequently, here, we showed for the first time that  $\text{Ti}_{0.8}\text{O}_2$  nanosheets could distinctively induce anticancer activity in human non-small cell lung cancer cells and advanced lung cancer cells from patients. This effect was demonstrated in several lung cancer lines in comparison to common chemotherapeutic drugs used in lung cancer patients. The  $\text{Ti}_{0.8}\text{O}_2$  nanosheets significantly increased cancer cell death in a concentration-dependent manner (Fig. 2). Moreover, the  $\text{Ti}_{0.8}\text{O}_2$  nanosheets also mediated apoptosis in lung cancer cells in a concentration-dependent manner (Fig. 2I–N). Furthermore, SEM morphological analysis demonstrated that  $10 \mu\text{g}/\text{mL}$   $\text{Ti}_{0.8}\text{O}_2$  nanosheets initially changed the morphology, including the formation of stress fibers, while TEM analysis for characterization of the  $\text{Ti}_{0.8}\text{O}_2$  nanosheets in cells showed that the  $\text{Ti}_{0.8}\text{O}_2$  nanosheets could appropriately disperse into H460 cells more easily than in DP cells (Fig. 3B). A previous study showed that various types of nanoparticles (NPs) could be used to induce anticancer activity in cancer cells, such as copper oxide nanoparticles [43]. Next, we further examined whether the  $\text{Ti}_{0.8}\text{O}_2$  nanosheets could induce cell apoptosis in H460 and A549 cells. We found that the treatment of lung cancer cells with  $\text{Ti}_{0.8}\text{O}_2$  nanosheets resulted in a significant induction of p53, which may, at least in part, play a role in  $\text{Ti}_{0.8}\text{O}_2$  nanosheets-mediated apoptosis (Fig. 3C and D). Consistent with our findings, a previous study showed that FePt/GO nanosheets suppressed proliferation and induced apoptosis in H1975 cells and silver nanoparticles induced apoptosis in human colon cancer cells mediated by p53 [44,45].

The majority of human cancers appear to exhibit either abnormal p53 or

395 disrupted p53 activation pathways. Intervention to restore wild-type p53 activities is  
396 an attractive approach for cancer therapy [46]. Interestingly, in this study, we further  
397 confirmed that  $\text{Ti}_{0.8}\text{O}_2$  nanosheets also had cytotoxicity in patient-derived primary  
398 lung cancer cells, with a lower  $\text{IC}_{50}$  compared to some other first-line  
399 chemotherapeutic drugs tested (Fig. 4). In addition, we have provided supportive  
400 information explaining that the cancer cell selectivity of  $\text{Ti}_{0.8}\text{O}_2$  nanosheets may be  
401 caused through the generation of superoxide anions, like in a previous study [20].  
402 Another previous study suggested that the effect of nanosilver on apoptosis was via  
403 ROS generation and the JNK-dependent pathway [47]. In addition, aminoflavone (AF)  
404 induced cell death in MCF-7 and MDA-MD-468 breast cancer cells, but it was not toxic  
405 to nonmalignant MCF-10A breast epithelial cells. Upon treatment with aminoflavone,  
406 an increase in intracellular ROS was detected correlated with an increased activation  
407 of caspase 3 and subsequent apoptosis. Further, the inhibition of ROS generation by  
408 pretreatment of the cells with N-acetyl-L-cysteine (NAC) reversed aminoflavone-  
409 induced cell death [48,49]. However, the generation of ROS was not associated with  
410 lung cancer cell death when the cells were pretreated with NAC or GSH and the cell  
411 viability of the cancer cells could not be reversed (Fig. 5C, D). This results suggests  
412 that the  $\text{Ti}_{0.8}\text{O}_2$  nanosheets may generate other ROS for inducing cell death. Therefore,  
413 we investigated the nitric oxide level in lung cancer cells because its activity could be  
414 associated with cell death, as previously described [16]. The results showed that the  
415 nitric oxide levels were increased in a concentration-dependent manner (Fig. 6A and  
416 C). Additionally, co-treatment with and/or PTIO (nitric oxide scavenger) and/or  
417 MnTBAP (superoxide anion inhibitor) inhibited  $\text{Ti}_{0.8}\text{O}_2$  nanosheets -induced cell death  
418 by increasing the cell viability. Much evidence has demonstrated that the direct  
419 toxicity of nitric oxide is modest, but can be greatly enhanced by reacting with the  
420 superoxide anion to form peroxynitrite ( $\text{ONOO}^-$ ), which can then damage DNA and  
421 inhibit DNA repair mechanisms [50,51].

422 p53 is an important tumor suppressor gene involved with the induction of  
423 apoptosis and cell cycle regulation in cells that have sustained DNA damage. We found  
424 that the generation of peroxynitrite after treatment with  $\text{Ti}_{0.8}\text{O}_2$  nanosheets  
425 upregulated the expression of p53-mediated apoptosis (Fig. 7). The data support the  
426 hypothesis that peroxynitrite contributes to the tumorigenic properties of p53  
427 mutations. Peroxynitrite was found to induce mitochondrial permeability transition  
428 changes and promote apoptosis in cell-free systems containing mitochondria [52].  
429 Cancer predisposition, onset, and therapeutic response can be critically determined  
430 by the integrity of the tumor suppressor p53. The degradation of p53 in normal cells  
431 is regulated through ubiquitination by the E3 ubiquitin ligase Mdm2 [53]. In this  
432 study, we found that under  $\text{Ti}_{0.8}\text{O}_2$  nanosheets treatment, the half-life of p53 was  
433 dramatically increased. The cycloheximide-based assay showed that the half-life of  
434 p53 in response to 10  $\mu\text{g}/\text{ml}$   $\text{Ti}_{0.8}\text{O}_2$  nanosheets was about 60 min in comparison to  
435 30–40 min in the non-treated control cells (Fig. 8A–C). After applying the selective  
436 proteasome inhibitor (MG132), we monitored the levels of the p53–ubiquitin complex  
437 and found that the formation of the complex was dramatically decreased in the  $\text{Ti}_{0.8}\text{O}_2$   
438 nanosheets -treated cancer cells (Fig. 8D and E). Here, we have revealed novel  
439 information regarding the role of reactive nitrogen species, especially peroxynitrite, in  
440 the regulation of p53 tetramerization. Our results showed that when the cells were  
441 exposed to the nanosheets, the intracellular level of peroxynitrite was highly  
442 upregulated (Fig. 6). Concomitantly, increased p53 was detected (Fig. 7A–C) with the  
443 decrease in p53–ubiquitin complex (Fig. 8D and E), implying that the upregulation of  
444 p53 occurs as a result of preventing its degradation process.

445 Peroxynitrite is considered an important biological inducer via its direct  
446 interaction with the protein in S-nitrosylation. S-nitrosylation is a rapid interaction  
447 wherein nitric oxide is attached to a thiol moiety of the target protein forming S-NO at  
448 the cysteine amino acid [54]. Until recently, more than 1000 proteins had been found  
449 as the targets of S-nitrosylation [55] and it was noted that such protein modification  
450 resulted in a profound alteration of the protein–protein interaction, protein function,  
451 protein localization, and protein stability [56]. Cellular stress, such as through  
452 cisplatin (CDDP) treatment, activates and stabilizes p53 via phosphorylation at the  
453 sites of Ser 15 and/or Ser 20, subsequently blocking p53–Mdm2 interaction and

454 suppressing p53 degradation [57]. Protein p53 is a key transcription factor that  
455 induces cell arrest when DNA is damaged and triggers the expression of DNA repair  
456 machinery, or apoptosis when the damage is irreversible [58]. The protein folds into  
457 several domains, the most relevant ones being the DNA-binding domain (p53DBD), at  
458 the core of the protein, and the tetramerization domain (p53TD), close to the C  
459 terminus [59]. However, the activity of the protein strongly depends on its tetrameric  
460 integrity [60]. Hence, molecules able to stabilize the tetrameric structure of mutated  
461 proteins with compromised tetramerization abilities could be valuable therapeutical  
462 tools. Furthermore, we report additional studies on the role of hydrogen bond  
463 interactions in protein stability and on the key binding residues of p53 to direct the  
464 effect of the *S*-nitrosylation (Fig. 9). In globular proteins, there are intermolecular  
465 hydrogen bonds between the protein and water molecules, and between water  
466 molecules that are bound with the proteins [61]. Here we used computational tools to  
467 predict the point of *S*-nitrosylation on the p53 protein, and found that peroxy  
468 nitrite may directly control p53 by *S*-nitrosylation to stabilize the tetrameric structure of this  
469 protein. To estimate the contribution of these hydrogen bonds to the conformational  
470 stability of a protein compared with that of the native p53 and *S*-nitrosylation of p53  
471 [62], we investigated the relationship between *S*-nitrosylation and the increase in p53  
472 stability. We identified the H-bond intermolecular interactions between a monomer of  
473 native p53 compared to its *S*-nitrosylation form, and found a higher stability of the  
474 tetrameric protein-protein complex in comparison to the native p53, especially  
475 regarding the reactivity of the cysteine at residue 182 in p53. The high reactivity of  
476 specific cysteine thiol groups in p53 are likely important for the regulation of p53 and  
477 its degradation pathways [38]. Moreover, peroxy nitrite has been shown to activate  
478 the opening of mitochondrial pores that release cytochrome c into the cytoplasm [63].  
479 According to our results, we found that peroxy nitrite induces p53 stability, and  
480 increases the activation of Bax and subsequently caspase 3. These changes are all  
481 hallmarks of cell death. Further, the nanosheets were shown to generate peroxy nitrite  
482 in aggressively driven mechanisms, including the process for the  
483 *S*-nitrosylation of p53 for protein stabilization. This novel finding on the role of Ti<sub>0.8</sub>O<sub>2</sub>  
484 nanosheets in p53-mediated apoptosis may have important implications in cancer  
485 treatment.  
486

## 487 Conclusions

488 In conclusion, our present study, for the first time provides information on the effect  
489 of Ti<sub>0.8</sub>O<sub>2</sub> nanosheets induce apoptosis through a molecular mechanism involving  
490 peroxy nitrite generation. After treatment with Ti<sub>0.8</sub>O<sub>2</sub> nanosheets, it may directly  
491 control p53 by *S*-nitrosylation to stabilize the tetrameric structure of this protein.  
492 This reflected that the *S*-nitrosylated at C182 of p53 resulted in a higher stability of  
493 the tetrameric protein-protein complex compared to the native p53. Therefore, the  
494 results of this study ingeminate the novel mechanism of action of nanomaterials for  
495 cancer therapy.  
496  
497

## 498 Methods

### 499 Ti<sub>0.8</sub>O<sub>2</sub> nanosheets synthesis and characterization

500 The Ti<sub>0.8</sub>O<sub>2</sub> nanosheets were prepared as reported previously. Briefly, the potassium  
501 zinc titanate K<sub>0.8</sub>Zn<sub>0.4</sub>Ti<sub>1.6</sub>O<sub>4</sub> was first synthesized by heating the stoichiometric  
502 mixture of K<sub>2</sub>CO<sub>3</sub>, ZnO and TiO<sub>2</sub> at 900 °C for 20 h. Then, the solid was soaked in 1 M  
503 HCl overnight (solid-to-solution ratio of 1 g-to-100 mL) for a total of 3 cycles, with the  
504 fresh acid replaced in between. The product is H<sub>1.6</sub>Ti<sub>1.6</sub>O<sub>4</sub>•0.8H<sub>2</sub>O, where 0.8H<sup>+</sup> first  
505 exchanged for 0.8K<sup>+</sup>, another 0.8H<sup>+</sup> for the leached [21] 0.4Zn<sup>2+</sup>, with water inclusion.  
506 Finally, 0.4 of the protonic form was mechanically shaken at 180 rpm for 14 days with  
507 diluted tetrabutylammonium hydroxide (TBAOH) solution (1 M, Sigma-Aldrich). The  
508 solid-to-solution was fixed at 0.4 g-to-100 mL, and the TBA<sup>+</sup>/H<sup>+</sup> ratio at 1. The white  
509 colloid of Ti<sub>0.8</sub>O<sub>2</sub> nanosheets was then obtained.

510 The absorption characteristics of the nanosheets colloid was measured using a  
511 T90+ UV/VIS spectrometer (PG Instruments). The “size” of the nanosheets (i.e., the

hydrodynamic radius as determined by Dynamic Light Scattering), and also the zeta potential, were measured using a Beckman Coulter Delsa Nano instrument. The nanosheets were also imaged using a JEOL JEM 2010 transmission electron microscope. Other results can be found in more detail elsewhere.

#### **Cell culture and reagents**

Non-small cell lung cancer cell lines including H460, H292, H23 and A549 were obtained from the American Type Culture Collection (Manassas, VA, USA). Human dermal papilla primary cell (primary DP1) was purchased from Celprogen (Benelux, Netherlands). The immortalized dermal papilla cells (DP) and human primary hair follicle dermal papilla cells (primary DP2) were purchased from Applied Biological Materials Inc) Richmond, BC. Furthermore, the human keratinocyte cell line (HaCaT) was purchased from Cell Lines Service (Heidelberg, Germany). H460, H292 and H23 cells were cultured in RPMI 1640 medium (Gibco, Grand Island, NY, USA), whereas A549, HaCaT, DP, primary DP1 and DP2 cells were cultivated DMEM medium (Gibco, Grand Island, NY, USA). The medium was supplemented with 10% fetal bovine serum (FBS), 100 units/ml penicillin/streptomycin and 2 mM L-glutamine (Gibco, MD, USA). The cells were incubated in a 5% CO<sub>2</sub> environment at 37°C. Phosphate buffer saline (PBS) and trypsin-EDTA were purchased from GIBCO (Grand Island, NY, USA). 3-(4,5-dimethylthiazol-2-yl)-2,5-diphenyltetrazoliumbromide (MTT), dimethyl sulfoxide (DMSO), Hoechst33342, propidium iodide (PI), bovine serum albumin (BSA) and dihydroethidium (DHE) were purchased from Sigma Chemical, Inc. (St. Louis, MO, USA). Apoptosis Kit (FITC) was purchased from ImmunoTools (Germany). DCF, 2',7'-Dichlorofluorescein; and 3'-p-(hydroxyphenyl) fluorescein (HPF) were purchased from Invitrogen (USA). Mn(III)tetrakis (4-benzoic acid) porphyrin (MnTBAP) was purchased from Merck (Germany). Antibody for mTOR, p53, Bcl-2, Mcl-1, Bax, caspase3 and β-actin as well as peroxidase-conjugated secondary antibodies were obtained from Cell Signaling Technology, Inc. (Danvers, MA).

#### **Patient-derived primary lung cancer cell line preparation from malignant pleural effusion**

The patient-derived malignant cancer cells were isolated from pleural effusions of recurrent or advanced stage non-small cell lung cancer patients who had been diagnosed at the King Chulalongkorn Memorial Hospital. The protocol was approved by the Ethics Committee of the Faculty of Medicine, Chulalongkorn University, Bangkok, Thailand (IRB 365/62) and was obtained informed consents from all contributors. Primary cancer cells were collected from pleural effusion (500-1,000 mL) through thoracentesis. The collected samples were centrifuged at 300 g for 10 min, at 4°C and the cells were resuspended in RPMI medium with 10% FBS, 2 mM L-glutamine, and 100 units/ml of each of penicillin and streptomycin. After culturing for 10-15 passages, they were characterized as the patient-derived primary cancer cell lines (PM-4, ELC09, ELC12, ELC16, ELC17, and ELC20).

#### **Cytotoxicity assay**

Cells were seeded onto 96-well plates at the density of  $1 \times 10^4$  cells/well and were allowed to incubate overnight. Then, cells were treated with various concentrations (0-100 µg/mL) of Ti<sub>0.8</sub>O<sub>2</sub> nanosheets for 24 h. at 37 °C and analyzed for cell viability using 3-(4,5-dimethylthiazol-2-yl)-2,5-diphenyltetrazolium bromide (MTT) assay. The MTT product was measured at 570 nm using a microplate reader. The cell viability was calculated by dividing the absorbance of the treated cells by that of the control cells and represented in percentage. All analyses were performed in 3 independent replicate cell cultures.

#### **Nuclear staining assay**

To determine apoptotic and necrotic cell death, H460 and A549 cells were seeded onto 96-well plates at the density of  $1 \times 10^4$  cells/well, were incubated overnight and then were treated with Ti<sub>0.8</sub>O<sub>2</sub> nanosheets at various concentrations (0–10 µg/mL) for 24 h. at 37 °C. After that, the cells were incubated with Hoechst 33342 (10 µg/mL) and propidium iodide (PI) (5 µg/mL) for 30 min at 37 °C in the dark. These cells were

571 imaged under a fluorescence microscope (Nikon ECLIPSE Ts2).

#### 572 **Cell apoptosis analysis**

573 Stage of apoptosis and necrosis cells were determined with Annexin V- FITC  
574 Apoptosis Kit (ImmunoTools, Germany). H460 and A549 cells were seeded in 24 well  
575 plates at a density of  $1 \times 10^5$  cells/mL and were treated with  $\text{Ti}_{0.8}\text{O}_2$  nanosheets at  
576 various concentrations (0–10  $\mu\text{g}/\text{mL}$ ) for 24 h. Then, cells were detached and  
577 suspended in 100  $\mu\text{L}$  of 1X binding buffer and incubated in 5  $\mu\text{L}$  of Annexin V-FITC and  
578 1  $\mu\text{L}$  of PI for 15 min at room temperature in the dark. Next, cells were analyzed by  
579 guava easyCyte™ flow cytometry systems.

#### 582 **Scanning electron microscopy (SEM) morphological analysis**

583 H460 treated cells were fix in 2.5% glutaraldehyde in 0.1 M phosphate buffer pH 7.2  
584 for 1-2 h. Then, the cells were rinsed with phosphate buffer and distilled water. Next,  
585 cells were dehydrated with a graded series of ethanol (30%, 50%, 70%, and 95% for 5  
586 minutes/each and 100% 3 times, 5 minutes/time), dried, mount and coat with gold  
587 (sputter coater, Balzers model SCD 040, Germany). Finally, cells were observed under  
588 a SEM (JEOL, model JSM6400, Japan).

#### 590 **Transmission electron microscopy (TEM) for cellular uptake analysis**

591 To confirm that  $\text{Ti}_{0.8}\text{O}_2$  nanosheets were uptake by cancer cell and/or normal cell,  
592 H460 and primary DP1 cells ( $1 \times 10^6$  cells/mL) were seeded and treated with  $\text{Ti}_{0.8}\text{O}_2$   
593 nanosheets at 10  $\mu\text{g}/\text{mL}$  for 24 h. Next, the treated cells were collected, washed with  
594 PBS and then fixed in 2% glutaraldehyde, post-fixed in 1% osmium tetroxide,  
595 dehydrated in alcohol and embedding. Thin sections of resin embedded cells were cut  
596 and observed cellular uptake with a transmission electron microscope (TEM) JEM-  
597 1400 (Jeol Ltd., Tokyo, Japan).

#### 598 **Western Blot Analysis**

600 Japan To determine proteins regulation in apoptosis pathway, the treated cells (H460  
601 and A549) were lysed into cellular lysates as previous described [20] Equal amounts  
602 of protein from each sample were separated by SDS-PAGE and transferred to 0.45  $\mu\text{m}$   
603 nitrocellulose membranes (Bio-Rad). The blots were blocked for 1 h. with 5 % non-fat  
604 dry milk in TBST (Tris-buffer saline with 0.1 % Tween containing 25 mM Tris-HCl (pH  
605 7.5), 125 mM NaCl and 0.1 % Tween 20) and incubated with specific primary  
606 antibodies against mTOR, p53, Bcl-2, Mcl-1, Bax, caspase3 and  $\beta$ -actin at 4 °C  
607 overnight. Then, the blots were washed in TBST and incubated with horseradish  
608 peroxidase (HRP)-conjugated secondary antibodies for 2 hours at room temperature.  
609 Finally, protein bands were detected using an enhancement chemiluminescence  
610 substrate (Supersignal West Pico; Pierce, Rockford, IL, USA) and exposed to film.

#### 611 **ROS, superoxide anion and hydroxyl radical detection by flow cytometry**

612 A549 and H460 cells were seeded in 24-well plate and incubated overnight. Then,  
613 DCFHDA, DHE and HPF were added and then incubated for 30 min in dark. Next, cells  
614 were treated with  $\text{Ti}_{0.8}\text{O}_2$  nanosheets for 3 h. Next, cells were washed and were  
615 resuspended in PBS. DCF fluorescence was quantified using guava easyCyte™ flow  
616 cytometry systems.

#### 617 **Nitric oxide detection by DAF-FM DA assay**

618 After detachment, cells were collected and incubated with 10  $\mu\text{M}$  DAF-FM DA for 30  
619 min at 37°C. The cells were then washed, resuspended in phosphate buffered saline,  
620 and analyzed for fluorescence intensity using guava easyCyte™ flow cytometry  
621 systems. These cells were imaged under a fluorescence microscope (Nikon ECLIPSE  
622 Ts2).

#### 623 **Immunofluorescence**

624 Cells were seeded onto 96-well plates at the density of  $1 \times 10^5$  cells/well. After  
625 treatment 24 h, the cells were fixed with 4% (w/v) paraformaldehyde for 30 min and  
626 permeabilized with 0.1% (v/v) Triton-X for 20 min. Next, the cells were incubated  
627

with 3% (w/v) BSA for 30 min, washed and incubated with an p53 or P-p53 antibody overnight at 4 °C, washed and incubated with Alexa Flour 488 (Invitrogen) conjugated goat anti-rabbit IgG (H+L) secondary antibody for 1 hour at room temperature in the dark. Therefore, the cells were washed with PBS, co-stained with 10 µg/mL Hoechst 33342 and visualized and imaged using fluorescence microscopy (Nikon ECLIPSE Ts2).

#### Cycloheximide (CHX) chasing assay

Cells were seeded and treated with 10 µg/mL of Ti<sub>0.8</sub>O<sub>2</sub> nanosheets with or without 50 µg/mL CHX for 0, 15, 30, 45, 60 and 90 min. The treated cells were collected and lysed with RIPA lysis buffer containing the protease inhibitor cocktail (Roche Diagnostics, Indianapolis, IN, USA). Western blot analysis was performed for detecting p53 protein levels. Protein bands were analyzed using the ImageJ software (version 1.52, National Institutes of Health, Bethesda, MD, USA), and the Mcl-1 protein half-life was calculated.

#### Immunoprecipitation Assay

Cells were seeded and treated with 0 and 10 µg/mL of Ti<sub>0.8</sub>O<sub>2</sub> nanosheets for 60 min. The treated cells were collected and lysed with RIPA lysis buffer containing the protease inhibitor cocktail (Roche Diagnostics, Indianapolis, IN, USA). After that, Immunoprecipitation was performed by using Dynabeads™ Protein G Immunoprecipitation Kit from Thermo Fisher Scientific Inc. (Waltham, MA, USA). Magnetic beads were prepared and resuspended with the primary antibody of p53 in a binding buffer for 10 min. A suspension of the magnetic bead-Ab complex was mixed with lysed protein and incubated at 4 °C overnight to allow p53 antigen to bind with magnetic bead-Ab complex. After that, the magnetic bead-Ab-Ag complex was washed three times using 200 µL washing Buffer, separated on the magnet between each wash, and the supernatant was removed. Elution Buffer was added for releasing the Ab-Ag complex from magnetic beads. The supernatant contained the Ab-Ag complex was then used to perform Western blot analysis for detecting the ubiquitinated p53 protein.

#### Computational method

The X-ray structure of tetrameric p53 core domain was taken from the protein data bank (PDB ID: 3KMD) [22]. The H++ web server [23] was used to assign the protonation state of all ionizable groups of amino acids at pH 7.4. The modeled protein was then submitted to all-atom molecular dynamics (MD) simulations using AMBER16 software package according to standard procedures [24-26] as summarized below. In brief, the starting structure of p53 protein was firstly energy-minimized using steepest descent (500 steps) and conjugated gradient (1,500 steps) based on the ff14SB AMBER force field [27] to reduce the unfavorable contacts. After that, the 100-ns MD simulation with the NPT ensemble at 310 K and 1 atm was carried out by the PMEMD module of AMBER16. The SHAKE algorithm [28] was applied to restrain the covalent bond involved in hydrogen atoms, allowing a simulation time step of 2 fs. The particle mesh Ewald [29] summation method was used to treat the long-range electrostatic interactions, whereas a nonbonded cutoff distance was set to 10 Å. The MD trajectories in production phase were collected every 10 ps and analyzed in terms of intermolecular hydrogen bonding interaction using the CPPTRAJ module [30] of AMBER 16. To determine the essential residues associated with protein-protein binding at the interface of the four monomers and the effect of the S-nitrosylation at the cysteine (Cys) residue towards the protein stability, the per-residue decomposition free energy ( $\Delta G_{\text{bind}}^{\text{residue}}$ ) based on the molecular mechanics/Poisson-Boltzmann surface area (MM/PBSA) method was performed using MMPBSA.py module [31] implemented in AMBER16.

#### Statistical Analysis

Data from three independent experiments are presented as mean ± standard error of mean (SEM). Multiple comparisons for statistically significant differences between multiple groups were performed using analysis of variance (ANOVA), followed by

Turkey's post hoc test. P value  $\leq 0.05$  will be considered as statistically significant.

#### Abbreviations

NSCLC: Non-small cell lung cancer; 2D: Two-dimensional; TEM: Transmission electron microscopy; SEM: Scanning electron microscopy; Bax: Bcl-2-associated X protein; Bcl-2: B-cell lymphoma 2; Mcl-1: Myeloid cell leukemia 1; C182: Cysteine residues at position 182; MDM2: Mouse double minute 2; mTOR: Mammalian target of rapamycin; TD: Tetramerization domain; NO: Nitric oxide; NOS: Nitric oxide synthases; HIF-1 $\alpha$ : Hypoxia-inducible factor-1 $\alpha$ ; O $_2^{\cdot-}$ : Superoxide anion; ONOO $^-$ : Peroxynitrite; DCF: 2',7'-dichlorofluorescein; DHE: dihydroethidium; FBS: fetal bovine serum; HPF: 3'-p-(hydroxyphenyl) fluorescein; MnTBAP: Mn(III)tetrakis (4-benzoic acid) porphyrin; MTT: 3-(4,5 dimethylthiazol-2-yl)-2,5-diphenyltetrazolium bromide; PBS: phosphate-buffered saline; PI: propidium iodide; DMSO: dimethyl sulfoxide; ROS: Reactive oxygen species; MD: Molecular dynamics; NAC: N-acetylcysteine; GSH: Glutathione; DAF-FM DA: Diaminofluorescein-FM diacetate; PTIO: 2-phenyl-4,4,5,5-tetramethylimidazole-1-oxyl 3-oxide; CHX: Cycloheximide; NPs: Nanoparticles.

#### Acknowledgements

This research was supported by a grant of the Thailand Research Fund through the Royal Golden Jubilee Ph.D. program (Grant No. PHD/0135/2559). The authors sincerely thank Cell-based Drug and Health Products Development Research Unit, Chulalongkorn University for their support in this study.

#### Funding

Grant No. PHD/0135/2559

#### Authors' contributions

Conceptualization—P.C.; Methodology—T.R., C.V., T.M., and P.C.; Formal analysis—R.S., B.N., and P.C.; Investigation—R.S., S.T., B.N., T.M., and P.C.; Writing and original draft preparation—R.S., S.T., T.M.; Writing, review, and editing—P.C.; Funding acquisition—P.C.; Supervision, P.C. All authors have read and agreed to the published version of the manuscript.

#### Availability of data and materials

The datasets used and/or analysed during the current study are available from the corresponding author on reasonable request.

#### Declarations

##### Ethics approval and consent to participate

All patient-derived malignant cancer cells experimental protocols were approved the Ethics Committee of the Faculty of Medicine, Chulalongkorn University, Bangkok, Thailand (IRB 365/62) and was obtained informed consents from all participants.

##### Consent for publication

Not applicable.

##### Competing interests

The authors declare that they have no competing interests.

#### Author details

<sup>1</sup>Interdisciplinary Program of Pharmacology Graduate School, Chulalongkorn University, Bangkok, Thailand. <sup>2</sup>Cell-based Drug and Health Products Development Research Unit, Chulalongkorn University, Bangkok, Thailand. <sup>3</sup>Departments of Pharmacology and Physiology, Faculty of Pharmaceutical Sciences, Bangkok, Thailand. <sup>4</sup>Department of Pharmacology, Faculty of Science, Mahidol University, Bangkok, Thailand. <sup>5</sup>Biocatalyst and Environmental Biotechnology Research Unit, Department of Biochemistry, Faculty of Science, Chulalongkorn University, Bangkok, Thailand. <sup>6</sup>Program in Bioinformatics and Computational Biology, Graduate School, Chulalongkorn University, Bangkok, Thailand. <sup>7</sup>Division of Medical Oncology, Department of Medicine, Chulalongkorn University, Bangkok, Thailand. <sup>8</sup>College of Materials Innovation and Technology, King Mongkut's Institute of Technology Ladkrabang, Bangkok, Thailand.

#### References

- Herbst RS, Morgensztern D, Boshoff C: The biology and management of non-small cell lung cancer. *Nature*. 2018;553(7689):446-454.
- Chen J: The Cell-Cycle Arrest and Apoptotic Functions of p53 in Tumor Initiation and Progression. *Cold Spring Harb Perspect Med*. 2016;6(3):a026104.
- Dai C, Gu W: p53 post-translational modification: deregulated in tumorigenesis. *Trends Mol Med*. 2010;16(11):528-536.
- Meeke DW, Anderson CW: Posttranslational modification of p53: cooperative integrators of function. *Cold Spring Harb Perspect Biol*. 2009;1(6):a000950.
- Zhang J, Huang K, O'Neill KL, Pang X, Luo X: Bax/Bak activation in the absence of Bid, Bim, Puma, and p53. *Cell Death Dis*. 2016;7:e2266.
- Tang D, Kang R, Berghe TV, Vandenabeele P, Kroemer G: The molecular machinery of regulated cell death. *Cell Res*. 2019;29(5):347-364.
- Chène P: The role of tetramerization in p53 function. *Oncogene*. 2001;20(21):2611-2617.
- Hainaut P, Milner J: Redox modulation of p53 conformation and sequence-specific DNA binding in vitro. *Cancer Res*. 1993;53(19):4469-4473.
- Buzek J, Latonen L, Kurki S, Peltonen K, Laiho M: Redox state of tumor suppressor p53 regulates its sequence-specific DNA binding in DNA-damaged cells by cysteine 277. *Nucleic Acids Res*. 2002;30(11):2340-2348.
- Scotcher J, Clarke DJ, Mackay CL, Hupp T, Sadler PJ, Langridge-Smith PRR: Redox regulation of tumour suppressor protein p53: identification of the sites of hydrogen peroxide oxidation and glutathionylation. *Chem. Sci*. 2013;4(3):1257-1269.
- Kim DH, Kundu JK, Surh YJ: Redox modulation of p53: mechanisms and functional significance. *Mol Carcinog*. 2011;50(4):222-234.
- Maillet A, Pervaiz S: Redox Regulation of p53, Redox Effectors Regulated by p53: A Subtle Balance. *Antioxid. Redox Signal*. 2011;16(11):1285-1294.
- Wilson G, Garthwaite J: Nitric Oxide. In: *Encyclopedia of Neuroscience*. edn. Edited by Squire LR. Oxford: Academic Press; 2009:1151-1156.
- Mengel A, Chaki M, Shekariesfahlan A, Lindermayr C: Effect of nitric oxide on gene transcription - S-nitrosylation of nuclear proteins. *Front Plant Sci*. 2013;4:293.
- Hess DT, Matsumoto A, Kim S-O, Marshall HE, Stamler JS: Protein S-nitrosylation: purview and parameters. *Nat. Rev. Mol. Cell Biol*. 2005;6(2):150-166.
- Radi R: Oxygen radicals, nitric oxide, and peroxynitrite: Redox pathways in molecular medicine. *PNAS*. 2018;115(23):5839.
- Pacher P, Beckman JS, Liaudet L: Nitric oxide and peroxynitrite in health and disease. *Physiol. Rev*. 2007;87(1):315-424.

- 765  
766  
767  
768  
769  
770  
771  
772  
773  
774  
775  
776  
777  
778  
779  
780  
781  
782  
783  
784  
785  
786  
787  
788  
789  
790  
791  
792  
793  
794  
795  
796  
797  
798  
799  
800  
801  
802  
803  
804  
805  
806  
807  
808  
809  
810  
811  
812  
813  
814  
815  
816  
817  
818  
819  
820  
821  
822  
823  
824  
825  
826  
827  
828  
829  
830  
831  
832  
833  
834  
835  
836  
837  
838  
839  
840  
841  
842
18. Boulaiz H, Alvarez PJ, Ramirez A, Marchal JA, Prados J, Rodriguez-Serrano F, Peran M, Melguizo C, Aranega A: Nanomedicine: application areas and development prospects. *Int J Mol Sci.* 2011;12(5):3303-3321.
  19. Zhang W, Yu J, Chang H: Two dimensional nanosheets as conductive, flexible elements in biomaterials. *J Mater Chem B.* 2015;3(25):4959-4964.
  20. Petpiroon N, Bhummapan N, Soonnarong R, Chantarakong W, Maluangnont T, Pongrakhananon V, Chanvorachote P: Ti<sub>0.8</sub>O<sub>2</sub> Nanosheets Inhibit Lung Cancer Stem Cells by Inducing Production of Superoxide Anion. *Mol. Pharmacol.* 2019;95(4):418-432.
  21. Long J, Hou Z, Shu C, Han C, Li W, Huang R, Wang J: Free-Standing Three-Dimensional CuCo<sub>2</sub>S<sub>4</sub> Nanosheet Array with High Catalytic Activity as an Efficient Oxygen Electrode for Lithium–Oxygen Batteries. *ACS Applied Materials & Interfaces.* 2019; 11(4):3834-3842.
  22. Cho Y, Gorina S, Jeffrey PD, Pavletich NP: Crystal structure of a p53 tumor suppressor-DNA complex: Understanding tumorigenic mutations. *Science.* 1994;265(5170):346-355.
  23. Anandkrishnan R, Aguilar B, Onufriev AV: H++ 3.0: Automating pK prediction and the preparation of biomolecular structures for atomistic molecular modeling and simulations. *Nucleic Acids Res.* 2012;40(W1):W537-W541.
  24. Nutho B, Rungrotmongkol T: Binding recognition of substrates in NS2B/NS3 serine protease of Zika virus revealed by molecular dynamics simulations. *J Mol Graph Model.* 2019;92:227-235.
  25. Meeprasert A, Hannongbua S, Kungwan N, Rungrotmongkol T: Effect of D168V mutation in NS3/4A HCV protease on susceptibilities of faldaprevir and danoprevir. *Mol Biosyst.* 2016;12(12):3666-3673.
  26. Boonma T, Nutho B, Rungrotmongkol T, Nunthaboot N: Understanding of the drug resistance mechanism of hepatitis C virus NS3/4A to paritaprevir due to D168N/Y mutations: A molecular dynamics simulation perspective. *Comput Biol Chem.* 2019;83.
  27. Maier JA, Martinez C, Kasavajhala K, Wickstrom L, Hauser KE, Simmerling C: ff14SB: Improving the Accuracy of Protein Side Chain and Backbone Parameters from ff99SB. *J Chem Theory Comput.* 2015;11(8):3696-3713.
  28. Ryckaert JP, Ciccotti G, Berendsen HJC: Numerical integration of the cartesian equations of motion of a system with constraints: molecular dynamics of n-alkanes. *J Comput Phys.* 1977;23(3):327-341.
  29. Darden T, York D, Pedersen L: Particle mesh Ewald: An N•log(N) method for Ewald sums in large systems. *J. Chem. Phys.* 1993;98(12):10089-10092.
  30. Roe DR, Cheatham TE: PTRAJ and CPPTRAJ: Software for processing and analysis of molecular dynamics trajectory data. *J Chem Theory Comput.* 2013;9(7):3084-3095.
  31. Miller III BR, McGee TD, Swails JM, Homeyer N, Gohlke H, Roitberg AE: MMPBSA.py: An efficient program for end-state free energy calculations. *J Chem Theory Comput.* 2012;8(9):3314-3321.
  32. Shafagh M, Rahmani F, Delirez N: CuO nanoparticles induce cytotoxicity and apoptosis in human K562 cancer cell line via mitochondrial pathway, through reactive oxygen species and P53. *Iran J Basic Med Sci.* 2015;18(10):993-1000.
  33. Kim Y-M, Bombeck Christopher A, Billiar Timothy R: Nitric Oxide as a Bifunctional Regulator of Apoptosis. *Circ. Res.* 1999;84(3):253-256.
  34. Vousden KH, Prives C: Blinded by the Light: The Growing Complexity of p53. *Cell.* 2009;137(3):413-431.
  35. Hollstein M, Sidransky D, Vogelstein B, Harris CC: p53 mutations in human cancers. *Science.* 1991;253(5015):49-53.
  36. Hainaut P, Hollstein M: p53 and human cancer: the first ten thousand mutations. *Adv Cancer Res.* 2000;77:81-137.
  37. Kao S-H, Wang W-L, Chen C-Y, Chang Y-L, Wu Y-Y, Wang Y-T, Wang S-P, Nesvizhskii AI, Chen Y-J, Hong T-M et al: Analysis of Protein Stability by the Cycloheximide Chase Assay. *Bio Protoc.* 2015;5(1):e1374.
  38. Schonhoff CM, Daou M-C, Jones SN, Schiffer CA, Ross AH: Nitric Oxide-Mediated Inhibition of Hdm2–p53 Binding. *Biochemistry.* 2002;41(46):13570-13574.
  39. Quader S, Kataoka K: Nanomaterial-Enabled Cancer Therapy. *Mol Ther : the journal of the American Society of Gene Therapy.* 2017;25(7):1501-1513.
  40. Patra JK, Das G, Fraceto LF, Campos EVR, Rodriguez-Torres MDP, Acosta-Torres LS, Diaz-Torres LA, Grillo R, Swamy MK, Sharma S et al: Nano based drug delivery systems: recent developments and future prospects. *J Nanobiotechnology.* 2018;16(1):71.
  41. Kulkarni M, Mazare A, Gongadze E, Perutkova S, kralj-iglic V, Milošev I, Schmuki P, Mozetic M: Titanium nanostructures for biomedical applications. *Nanotechnology.* 2015;26:062002.
  42. Wu S, Weng Z, Liu X, Yeung K, Chu P: Functionalized TiO<sub>2</sub> Based Nanomaterials for Biomedical Applications. *Adv. Funct. Mater.* 2014;24.
  43. Arunachalam K, Sankar R, Chidambaram A, Saravanan K, Aarthi K, Selvaraju K, Mathuram T, Ravikumar V: Copper oxide nanoparticles induce anticancer activity in A549 lung cancer cells by inhibition of histone deacetylase. *Biotechnol. Lett.* 2017;40.
  44. Ma S, Miao H, Luo Y, Sun Y, Tian X, Wang F, You C, Peng S, Tang G, Yang C et al: FePt/GO Nanosheets Suppress Proliferation, Enhance Radiosensitization and Induce Autophagy of Human Non-Small Cell Lung Cancer Cell. *slnt. J. Biol. Sci.* 2019;15(5):999-1009.
  45. Satapathy SR, Mohapatra P, Preet R, Das D, Sarkar B, Choudhuri T, Wyatt MD, Kundu CN: Silver-based nanoparticles induce apoptosis in human colon cancer cells mediated through p53. *Nanomedicine (Lond).* 2013;8(8):1307-1322.
  46. Haupt S, Haupt Y: Importance of p53 for cancer onset and therapy. *Anti-Cancer Drugs.* 2006;17(7).
  47. Hsin yh, Chen C-F, Huang S, Shih T-S, Lai P-S, Chueh P: The apoptotic effect of nanosilver is mediated by a ROS-and JNK-dependent mechanism involving the mitochondrial pathway in NIH3T3 cells. *Toxicol. Lett.* 2008;179:130-139.
  48. Loiza-Pérez AI, Kenney S, Boswell J, Hollingshead M, Alley MC, Hose C, Ciolino HP, Yeh GC, Trepel JB, Vistica DT et al: Aryl hydrocarbon receptor activation of an antitumor aminoflavone: basis of selective toxicity for MCF-7 breast tumor cells. *Mol Cancer Ther.* 2004;3(6):715-725.
  49. McLean L, Soto U, Agama K, Francis J, Jimenez R, Pommier Y, Sowers L, Brantley E: Aminoflavone induces oxidative DNA damage and reactive oxidative species-mediated apoptosis in breast cancer cells. *Int J Cancer.* 2008;122(7):1665-1674.
  50. Islam BU, Habib S, Ahmad P, Allarakha S, Moinuddin, Ali A: Pathophysiological Role of Peroxynitrite Induced DNA Damage in Human Diseases: A Special Focus on Poly(ADP-ribose) Polymerase (PARP). *Indian J Clin Biochem: IJCB.* 2015;30(4):368-385.
  51. Cobbs CS, Samanta M, Harkins LE, Gillespie GY, Merrick BA, MacMillan-Crow LA: Evidence for peroxynitrite-mediated modifications to p53 in human gliomas: possible functional consequences. *Arch. Biochem. Biophys.* 2001;394(2):167-172.
  52. Pryor WA, Squadrito G: The chemistry of peroxynitrite: A product from the reaction of nitric oxide with superoxide. *Am. J. Physiol.* 1995;268:L699-722.
  53. Chao C, Saito S, Kang J, Anderson CW, Appella E, Xu Y: p53 transcriptional activity is essential for p53-dependent apoptosis following DNA damage. *Embo j.* 2000;19(18):4967-4975.
  54. Sun J, Steenbergen C, Murphy E: S-nitrosylation: NO-related redox signaling to protect against oxidative stress. *Antioxid. Redox Signal.* 2006;8(9-10):1693-1705.
  55. Stamler JS, Hess DT: Nascent nitrosylases. *Nat. Cell Biol.* 2010;12(11):1024-1026.
  56. Nakamura T, Tu S, Akhtar MW, Sunico CR, Okamoto S-I, Lipton SA: Aberrant protein s-nitrosylation in neurodegenerative diseases. *Neuron.* 2013;78(4):596-614.
  57. Imamura K, Ogura T, Kishimoto A, Kaminishi M, Esumi H: Cell cycle regulation via p53 phosphorylation by a 5'-AMP activated protein kinase activator, 5-aminoimidazole-4-carboxamide-1-beta-D-ribofuranoside, in a human hepatocellular carcinoma cell line. *Biochem Biophys Res Commun.* 2001;287(2):562-567.
  58. Levine AJ: p53, the cellular gatekeeper for growth and division. *Cell.* 1997;88(3):323-331.
  59. Joergers AC, Fersht AR: Structure-function-rescue: the diverse nature of common p53 cancer mutants. *Oncogene.* 2007;26(15):2226-2242.
  60. Chène P: The role of tetramerization in p53 function. *Oncogene.* 2001;20(21):2611-2617.
  61. Takano K, Yamagata Y, Funahashi J, Hioki Y, Kuramitsu S, Yutani K: Contribution of intra- and intermolecular hydrogen bonds to the conformational stability of human lysozyme(.). *Biochemistry.* 1999;38(39):12698-12708.

- 843  
844  
845  
846
62. Yamagata Y, Kubota M, Sumikawa Y, Funahashi J, Takano K, Fujii S, Yutani K: Contribution of hydrogen bonds to the conformational stability of human lysozyme: calorimetry and X-ray analysis of six tyrosine --> phenylalanine mutants. *Biochemistry*. 1998;37(26):9355-9362.
63. Brown GC, Borutaite V: Nitric oxide, cytochrome c and mitochondria. *Biochem Soc Symp*. 1999;66:17-25.

847

848

849

850

851

852

853

854

855

856

857

858

859

860

861

862

863

864

865

866

867

868

869

870

871

872

873

874

875

876

877

878

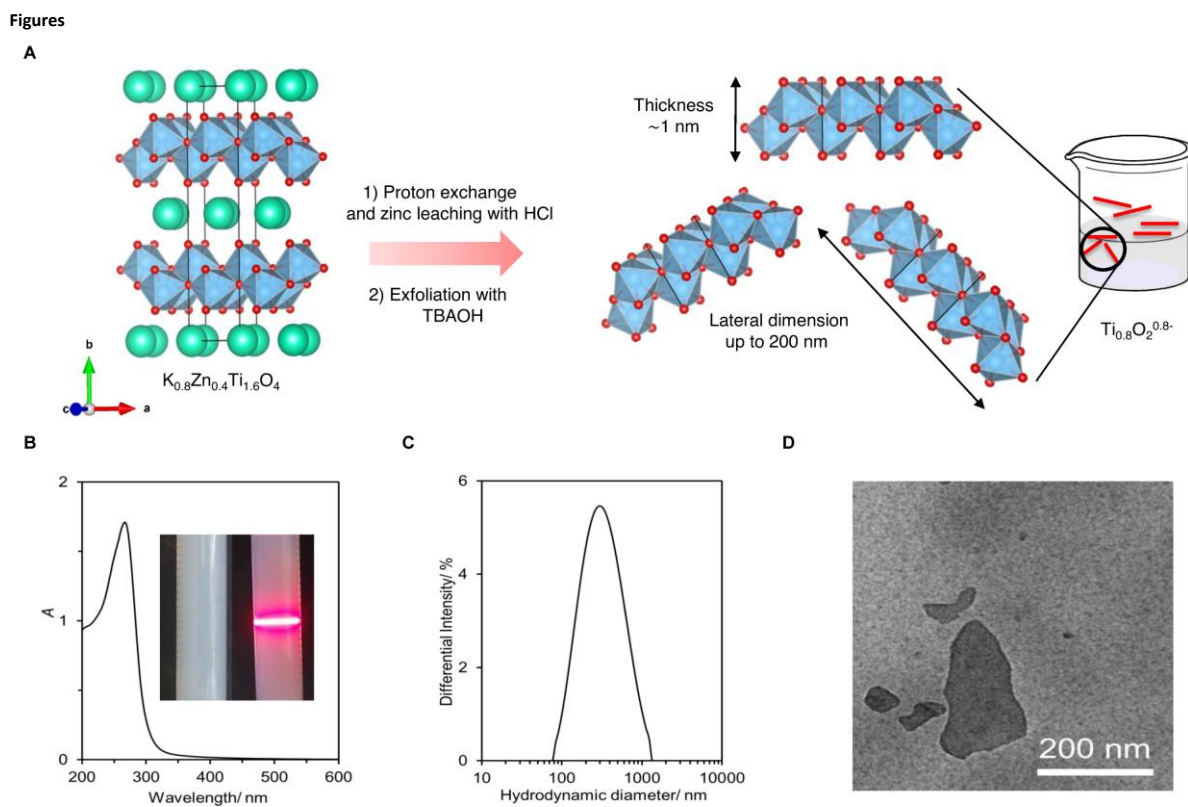
879

880

881

882

883



884

**Fig. 1** Synthesis and characterization of the  $Ti_{0.8}O_2$  nanosheets. **A** Schematic diagram of the  $Ti_{0.8}O_2$  nanosheets preparation. **B** UV-VIS absorption spectrum and photograph of the nanosheets without (left) and with (right) the laser light shining through. **C** Size of the nanosheets. **D** Representative TEM image of the deposited nanosheets.

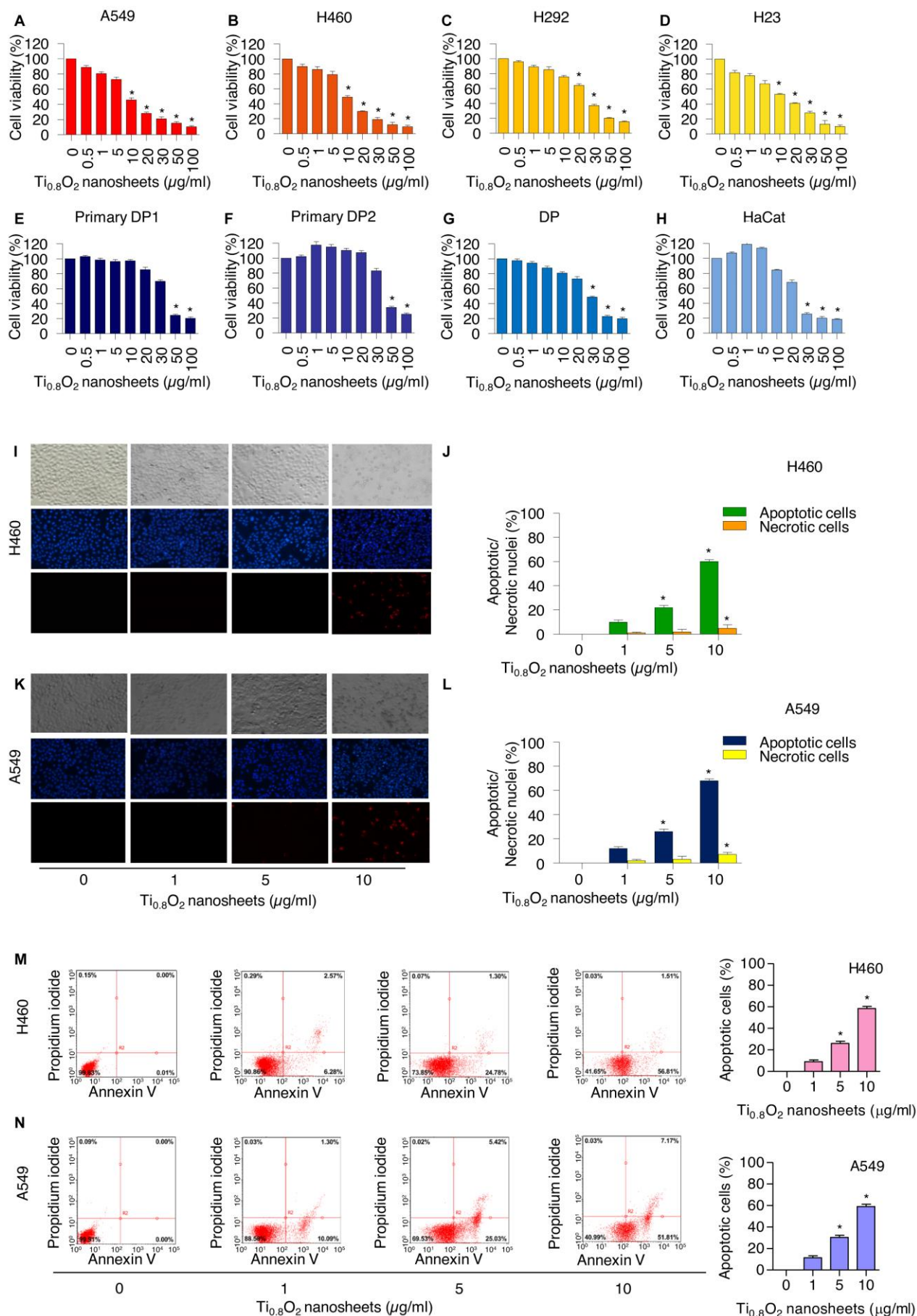


**Fig. 2** Cytotoxicity of the  $Ti_{0.8}O_2$  nanosheets on human lung cancer cells and normal cells. **A–H** Effect of the  $Ti_{0.8}O_2$  nanosheets on the cell viability of lung cancer cells (A549, H460, H292, and H23) and normal cells (Dermal Papilla (DP) cell line, primary DP1, primary DP2, and HaCaT keratinocyte cells) over 24 h using the MTT assay. **I–L** Morphology of the apoptotic nuclei stained with Hoechst 33342 dye and propidium iodide in cells treated with  $Ti_{0.8}O_2$  nanosheets, determined by visualization under a fluorescence microscope; the percentages of nuclear fragments and PI positive cells were calculated. **M, N** Apoptotic and necrotic cells were determined using annexin V-FITC/PI staining with flow cytometry. Data are shown as the mean  $\pm$  SD (n = 3). \* P < 0.05 versus non-treated control.

886

887

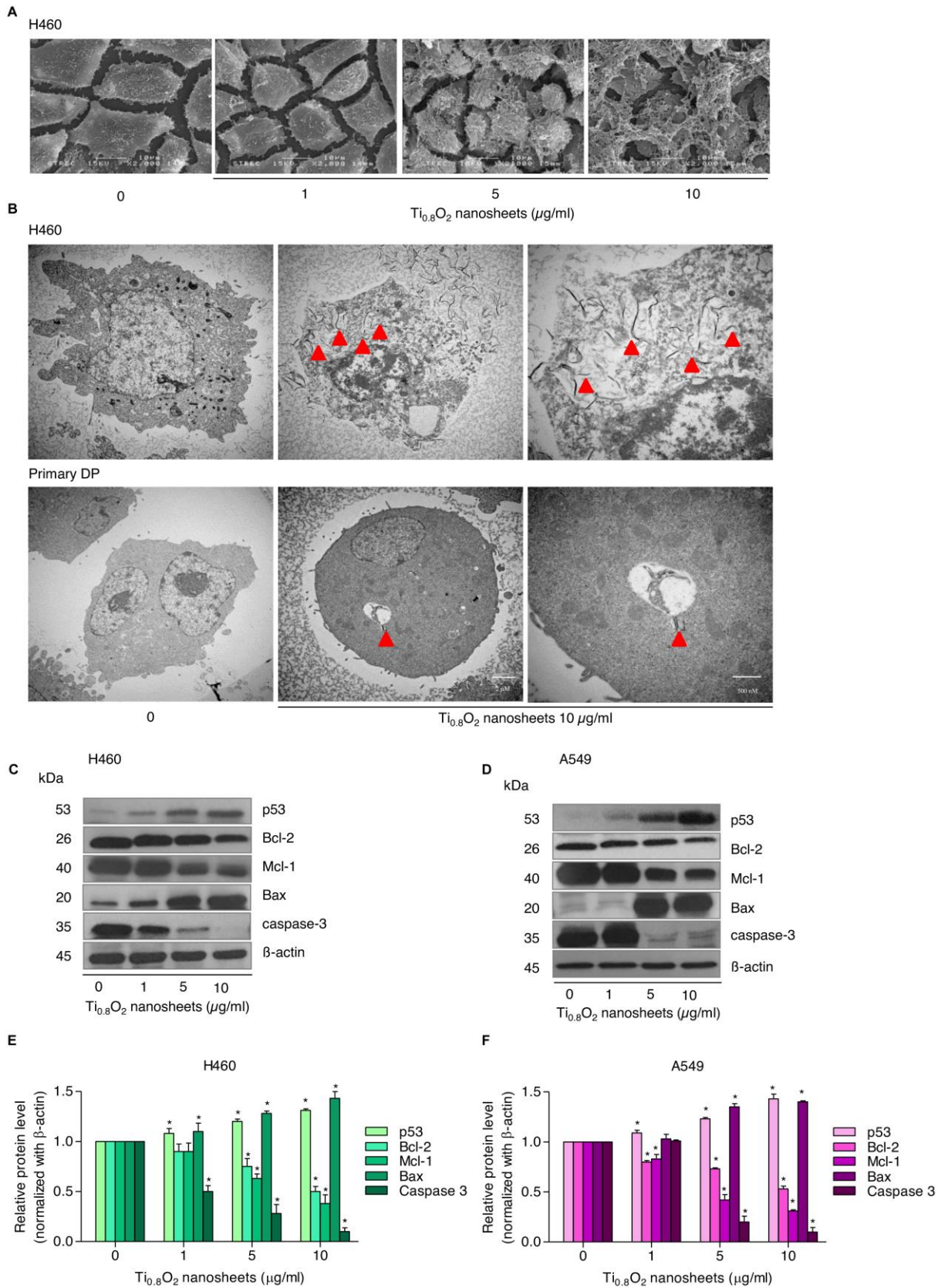


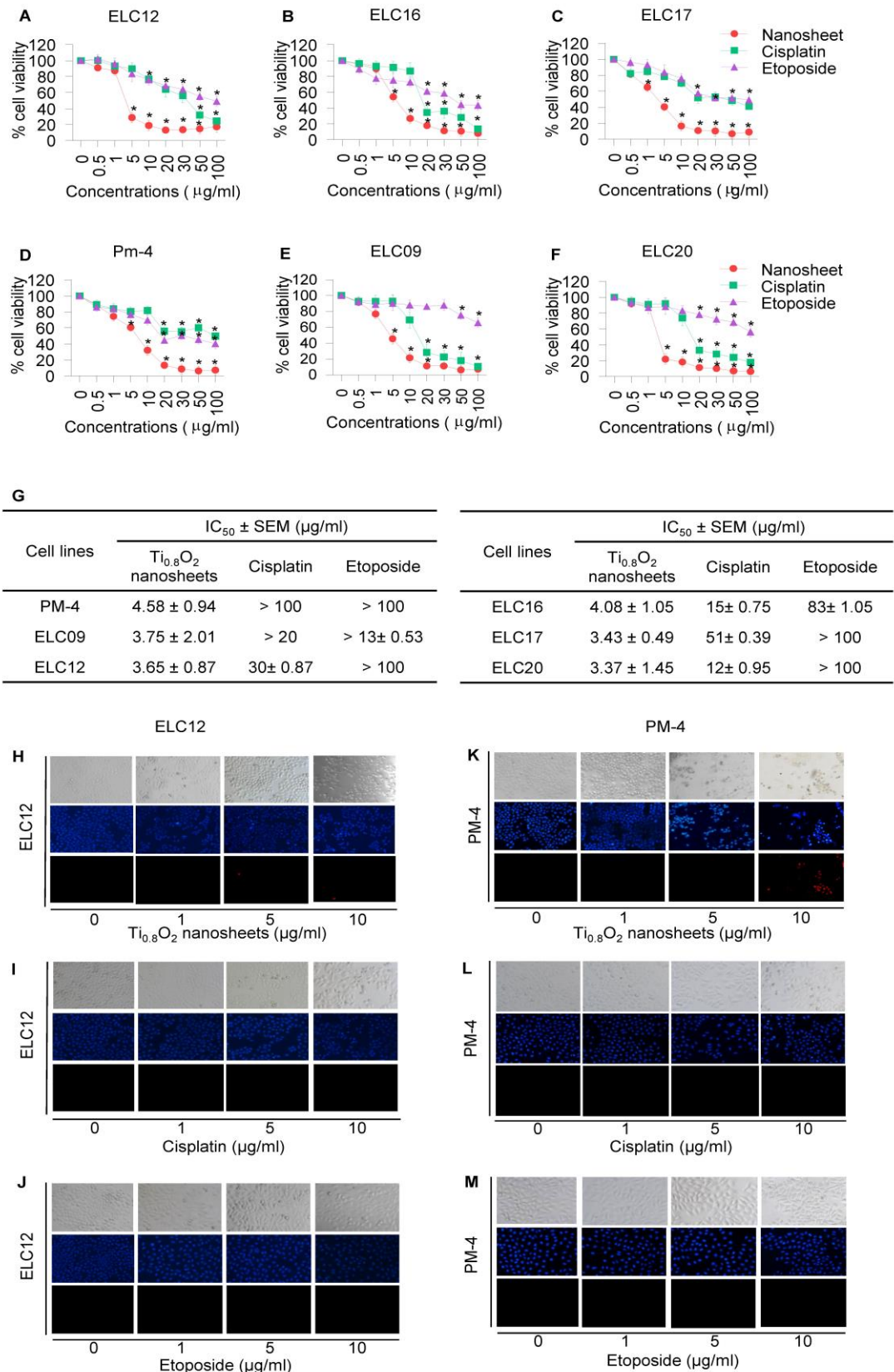
**Fig. 3** Morphology and characterization of cells when treated with Ti<sub>0.8</sub>O<sub>2</sub> nanosheets. **A** Morphology of H460 cells determined by scanning electron microscopy (SEM). **B** Cellular uptake of Ti<sub>0.8</sub>O<sub>2</sub> nanosheets in H460 and primary DP cells at 24 h determined by transmission electron microscopy (TEM). **C, D** Effect of Ti<sub>0.8</sub>O<sub>2</sub> nanosheets on apoptosis-related proteins measured by Western blot analysis. Blots were reprobed with β-actin to confirm the equal loading of samples. **E, F** Relative protein levels calculated by densitometry. Data are shown as the mean ± SD (n = 3). \* P < 0.05 versus non-treated control

888

889

890

891  
892  
893



894

**Fig. 4** Cytotoxicity of the Ti<sub>0.8</sub>O<sub>2</sub> nanosheets on malignant pleural effusion from advanced lung cancer patients. **A-F** Effect of the Ti<sub>0.8</sub>O<sub>2</sub> nanosheets on the cell viability of malignant pleural effusion for 24 h using the MTT assay to determine the IC<sub>50</sub> values. **G** Percentages of cell viability were determined using the MTT assay. **H-M** Morphology of apoptotic nuclei stained with Hoechst 33342 dye and propidium iodide in cells treated with Ti<sub>0.8</sub>O<sub>2</sub> nanosheets, cisplatin and etoposide were determined by visualization under a fluorescence microscope; the percentages of nuclear fragments and PI positive cells were calculated. Data are shown as the mean ± SD (n = 3). \* P < 0.05 versus non-treated control

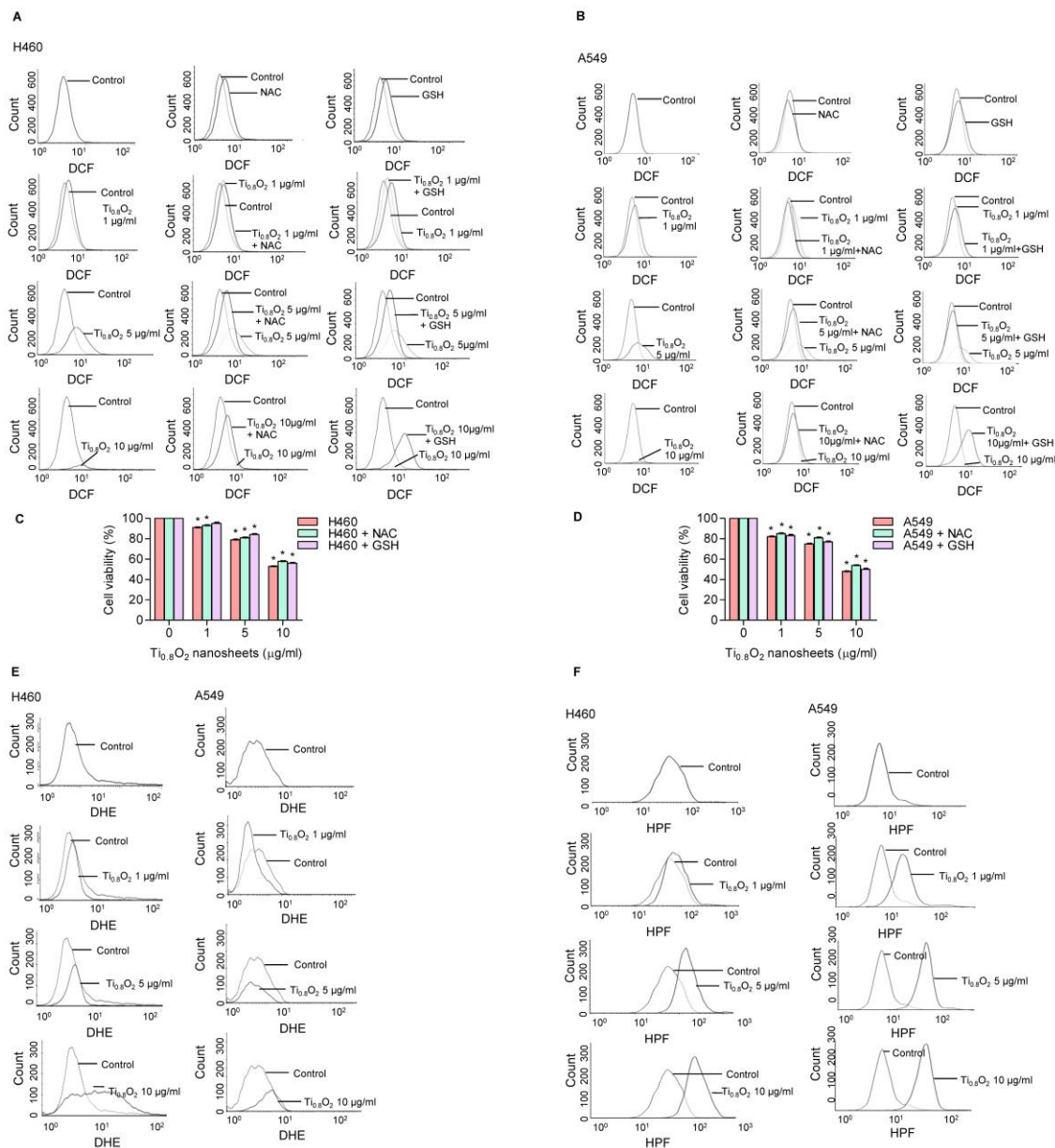


**Fig. 5**  $Ti_{0.8}O_2$  nanosheets induced intracellular ROS in H460 and A549 cells. **A, B** The effect of  $Ti_{0.8}O_2$  nanosheets (0–10  $\mu g/ml$ ) on intracellular ROS induction at 24 h in H460 and A549 cells was determined by flow cytometry with the fluorescent probe DCF (10  $\mu M$ ). Cells were treated with  $Ti_{0.8}O_2$  nanosheets (0–10  $\mu g/ml$ ) alone for 24 h or with the pretreatment of 2.5 mM NAC and 2.5 mM GSH. **C, D** Effect of  $Ti_{0.8}O_2$  nanosheets on cell viability in H460 and A549 cells at 24 h with the pretreatment of 2.5 mM NAC or 2.5 mM GSH was determined by the MTT assay. Data are shown as the mean  $\pm$  SD ( $n = 3$ ). **E** The effect of  $Ti_{0.8}O_2$  nanosheets (0–10  $\mu g/ml$ ) on superoxide anion induction at 24 h in H460 and A549 cells was determined by flow cytometry with the fluorescent probe DHE (10  $\mu M$ ). **F** The effect of  $Ti_{0.8}O_2$  nanosheets (0–10  $\mu g/ml$ ) on hydroxyl radical induction at 24 h in H460 and A549 cells was determined by flow cytometry with the fluorescent probe HPF (10  $\mu M$ ).

895

896

897

898

899

900

901

902

903

904

905

906

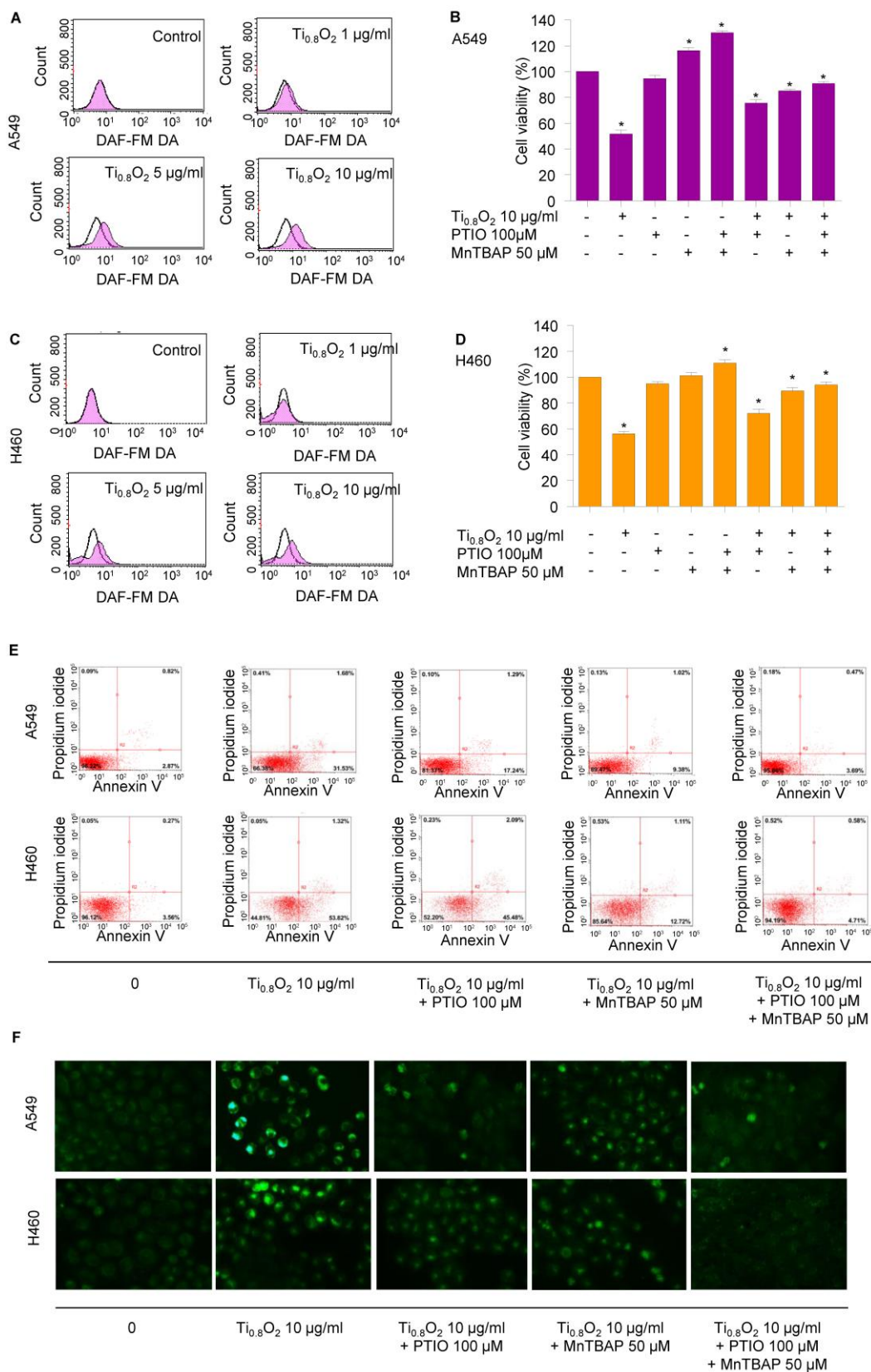


**Fig. 6**  $Ti_{0.8}O_2$  nanosheets induced NO in A549 and H460 cells and mediated peroxynitrite generation in these cells. **A, C** Effect of  $Ti_{0.8}O_2$  nanosheets on NO levels in A549 and H460 cells. Cells were treated with DAF-FM DA and various concentrations of  $Ti_{0.8}O_2$  nanosheets (0–10  $\mu g/ml$ ) for 30 min and the peroxynitrite levels were determined at 3 h by flow cytometry. **B, D** The cytotoxic effect of  $Ti_{0.8}O_2$  nanosheets and NO scavenger (PTIO) on A549 and H460 cells. Effect of  $Ti_{0.8}O_2$  nanosheets and NO scavenger (PTIO) (50  $\mu M$ ) or pretreatment with a superoxide inhibitor (MnTBAP) (50  $\mu M$ ) for 24 h by MTT assay. **E** Apoptotic and necrotic cells were determined using annexin V-FITC/PI staining with flow cytometry. **F** Cellular NO level stained with DAF-FM DA in cells treated with  $Ti_{0.8}O_2$  nanosheets (10  $\mu g/ml$ ) or pretreated with PTIO (100  $\mu M$ ) or pretreated with MnTBAP (50  $\mu M$ ) were determined by visualization under a fluorescence microscope.

907

908

909

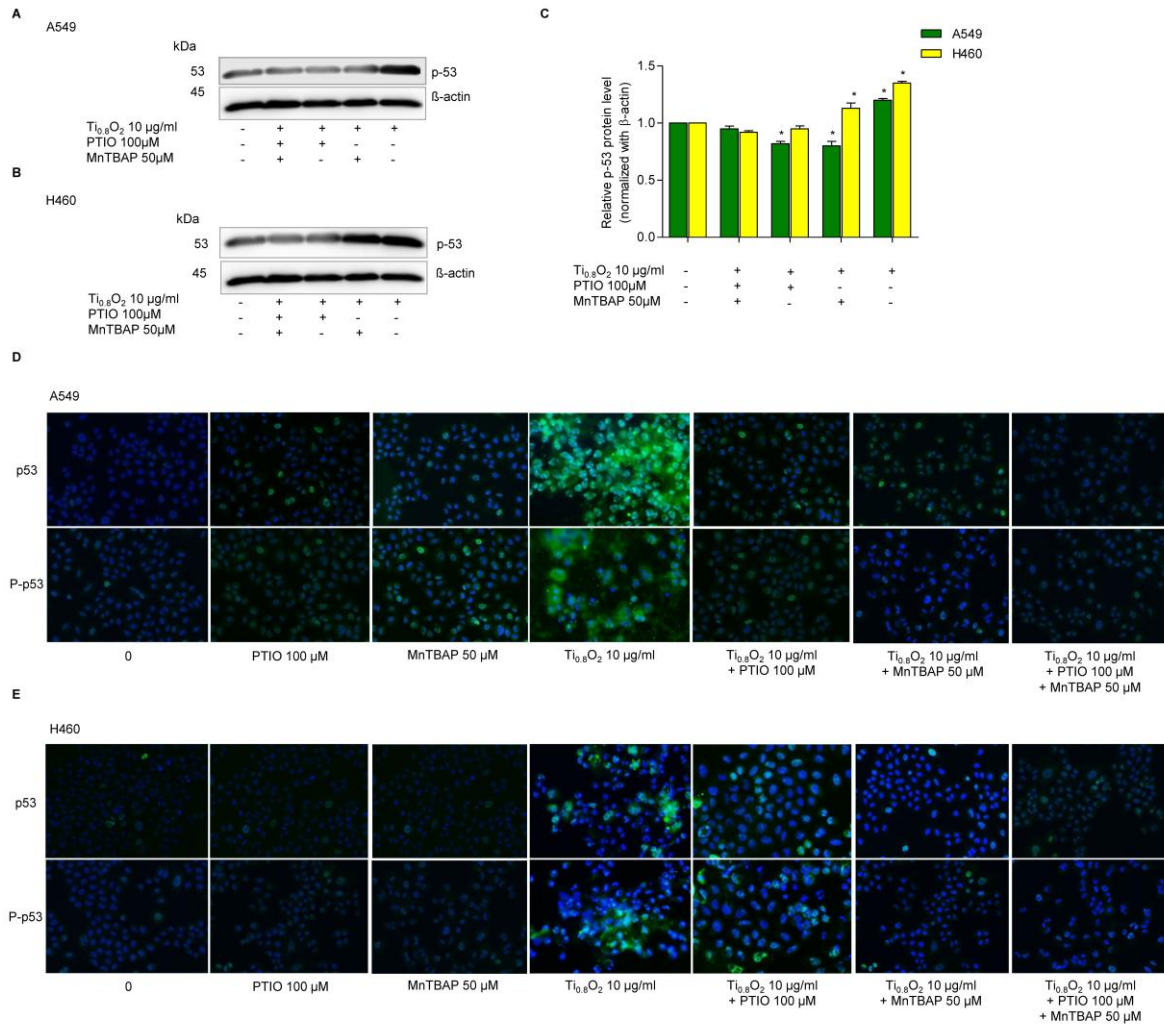


**Fig. 7**  $\text{Ti}_{0.8}\text{O}_2$  nanosheets associated with apoptosis in A549 and H460 cells via p53 upregulation. **A, B** Peroxynitrite-potentiated cell apoptosis through the p53 protein was measured by Western blot analysis. **C** Blots were reprobed with  $\beta$ -actin to confirm the equal loading of samples. The relative protein levels were calculated by densitometry. Data are shown as the mean  $\pm$  SD (n = 3). \* P < 0.05 versus non-treated control. **D, E** The expressions of p53 and P-p53 were analyzed by immunofluorescence staining in A549 and H460 cells.

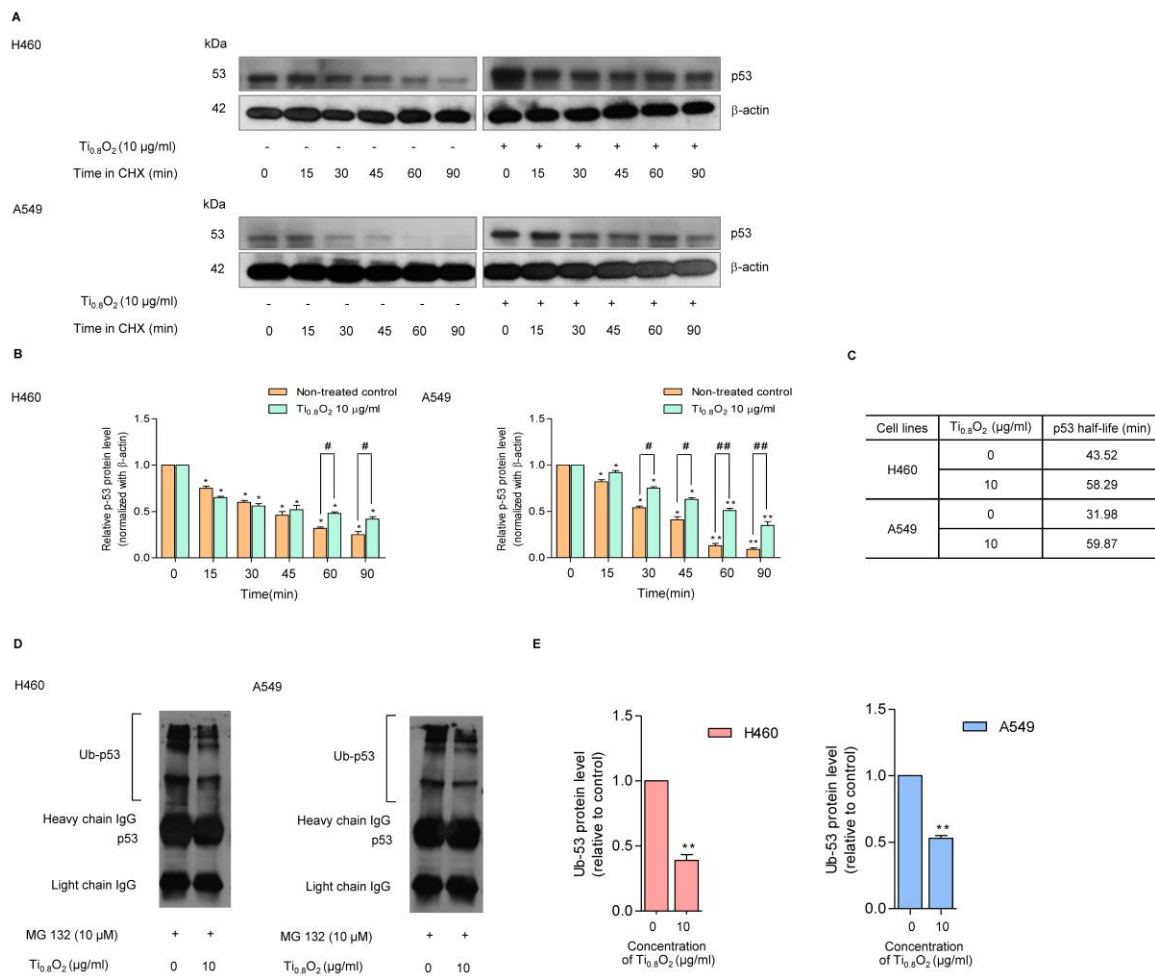


**Fig. 8**  $TiO_2O_2$  nanosheets increased p53 stability but not through the p53 proteasomal degradation. **A** The half-life of p53 was confirmed using the cycloheximine (CHX) chasing assay. H460 and A549 cell lines were treated with 50  $\mu$ g/ml of CHX with or without 10  $\mu$ g/ml  $TiO_2O_2$  nanosheets as indicated by the time in minutes. Western blot analysis was performed to evaluate the p53 protein level. **B** The relative p53 protein levels were calculated and compared with the non-treatment control at 0 min. **C** The half-lives of the p53 protein of H460 and A549 cells were calculated. **D** H460 and A549 cells were pretreated with 10  $\mu$ M MG132 for 30 min followed by treatment with 10  $\mu$ g/ml  $TiO_2O_2$  nanosheets for 60 min. The protein lysates were collected and incubated with a mixture of beads and p53 primary antibodies to pull out the protein of interest. Then, the ubiquitinated protein levels were measured by Western blot analysis. **E** Ub-p53 levels were quantified by densitometry. The statistical calculation was compiled with repeated measured one-way ANOVA with Scheff's post-hoc test for individual comparisons and the t-test for two group comparisons. The relative to control protein levels are reported. (n = 3) (\*p < 0.05, \*\*p < 0.01 compared with the untreated control at 0 min and # < 0.05, ## p < 0.01 compared with the untreated control at the same time).

911  
912

913  
914  
915  
916

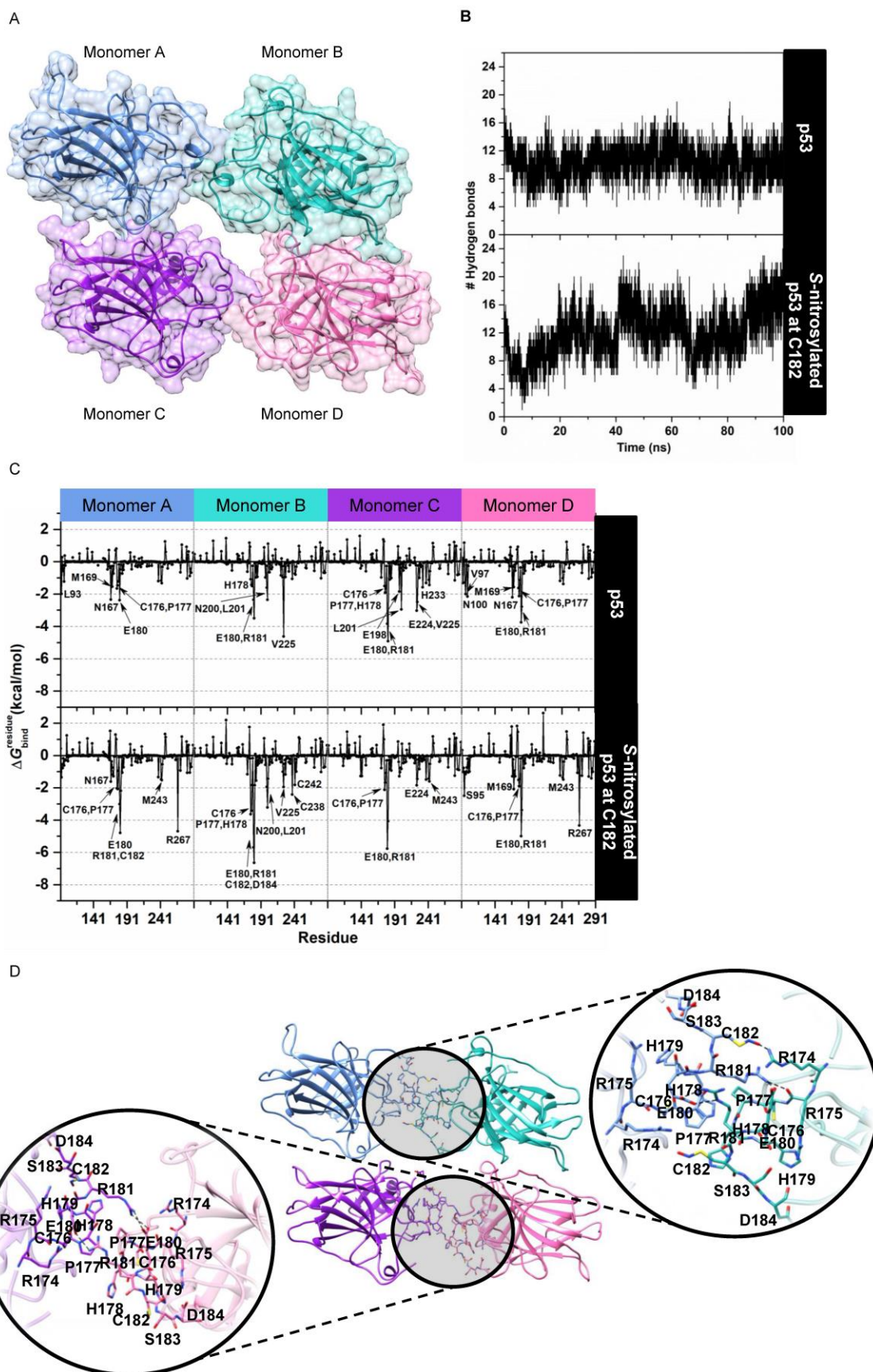


**Fig. 9** S-nitrosylation in the regulation of p53 stability. **A** Three-dimensional (3D) structure of the tetrameric p53 core domain without DNA bound (PDB ID: 3KMD). **B** Time evolution of the total number of intermolecular hydrogen bonds formed between each monomer of the p53 core domain and its adjacent monomer. **C** The plot of (kcal/mol) of the p53 tetramer for the native form (top) and the C182 S-nitrosylation (bottom) system. **D** The representative 3D structure taken from the last MD snapshot of the S-nitrosylation system, with hydrogen bonds and electrostatic interactions represented by black dashed lines.

# Figures

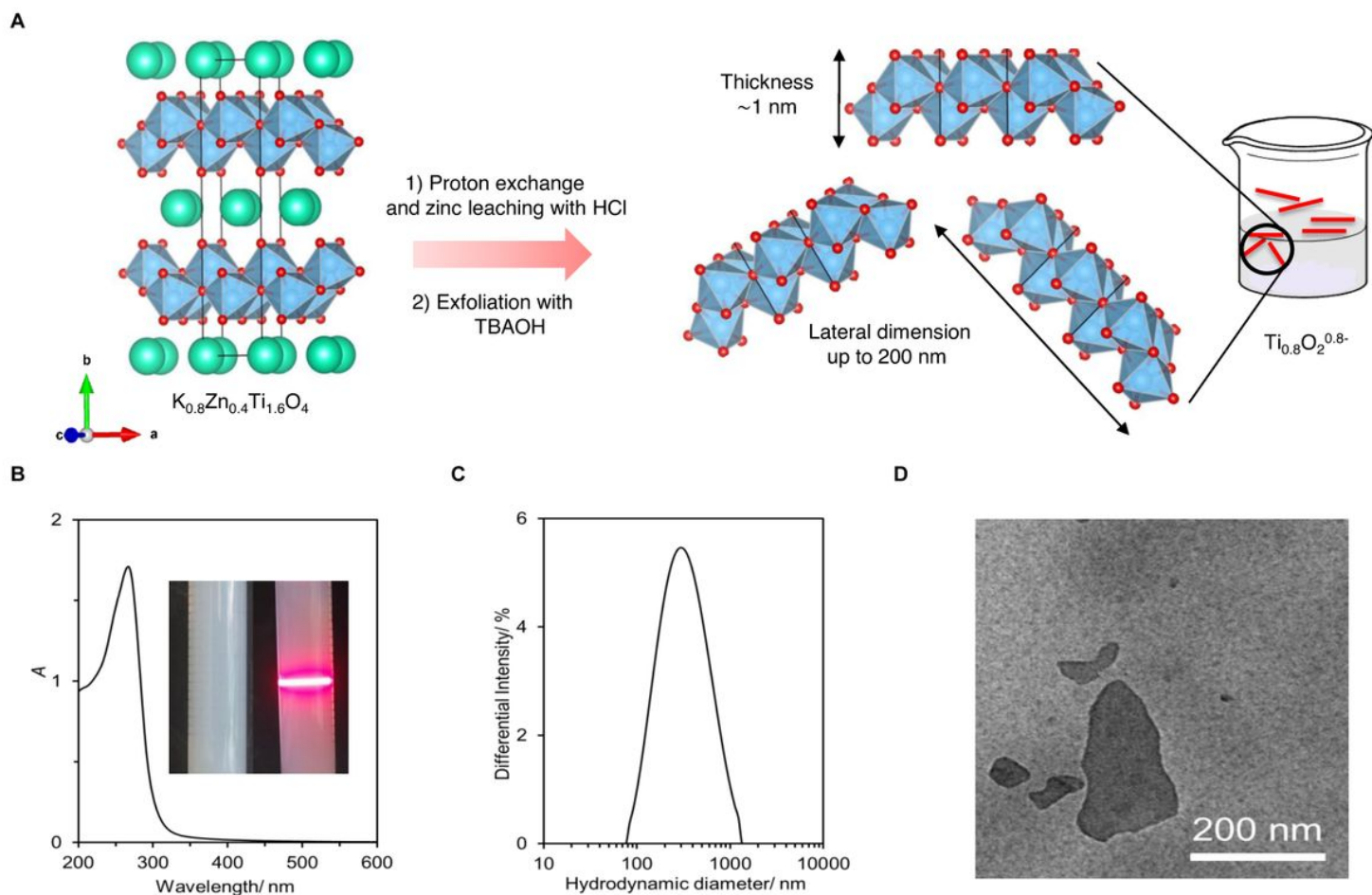


**Figure 1**

Synthesis and characterization of the  $Ti_{0.8}O_2$  nanosheets. A Schematic diagram of the  $Ti_{0.8}O_2$  nanosheets preparation. B UV-VIS absorption spectrum and photograph of the nanosheets without (left) and with (right) the laser light shining through. C Size of the nanosheets. D Representative TEM image of the deposited nanosheets.

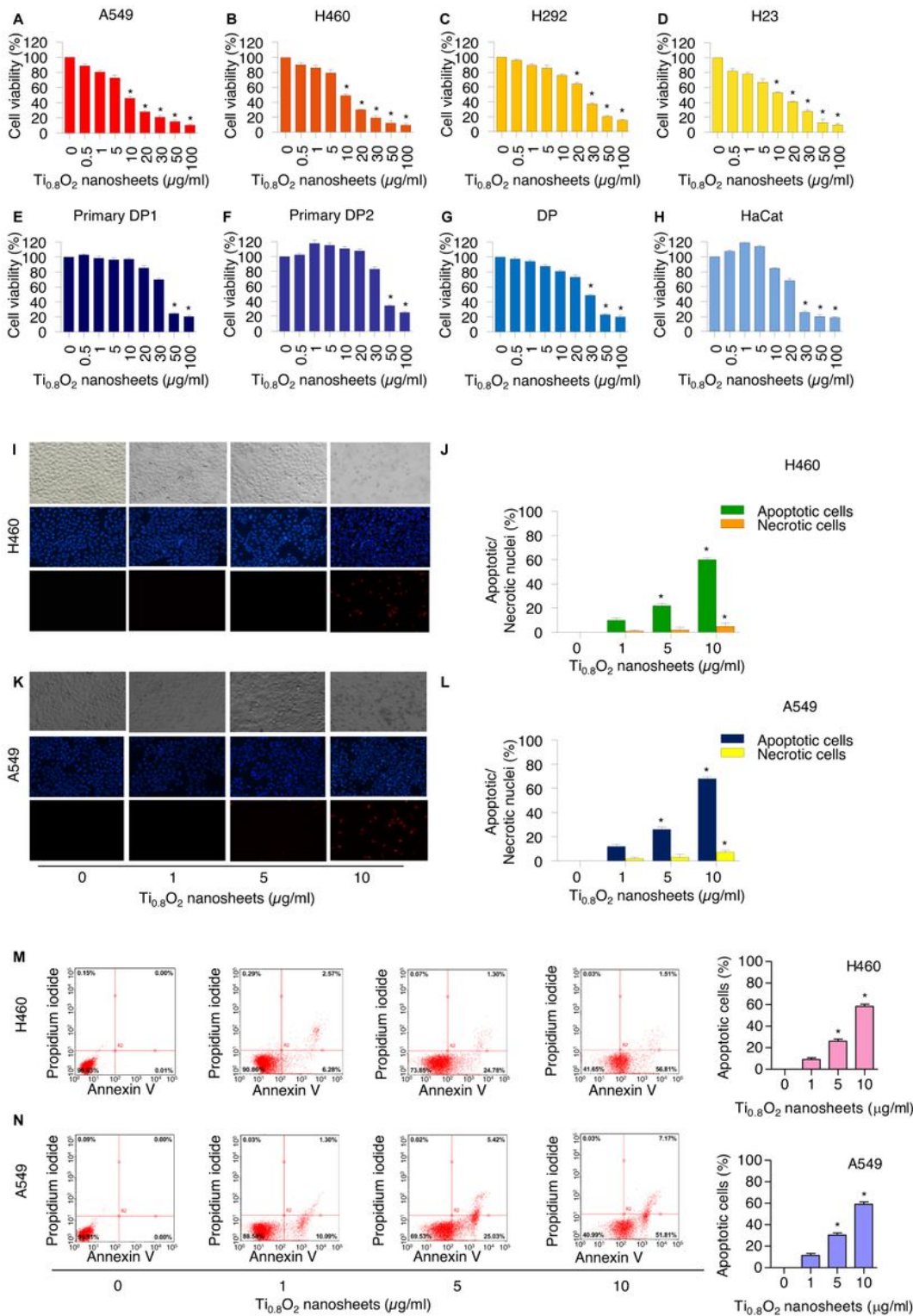


**Figure 2**

Cytotoxicity of the  $Ti_{0.8}O_2$  nanosheets on human lung cancer cells and normal cells. A–H Effect of the  $Ti_{0.8}O_2$  nanosheets on the cell viability of lung cancer cells (A549, H460, H292, and H23) and normal cells (Dermal Papilla (DP) cell line, primary DP1, primary DP2, and HaCaT keratinocyte cells) over 24 h using the MTT assay. I–L Morphology of the apoptotic nuclei stained with Hoechst 33342 dye and propidium iodide in cells treated with  $Ti_{0.8}O_2$  nanosheets, determined by visualization under a

fluorescence microscope; the percentages of nuclear fragments and PI positive cells were calculated. M, N Apoptotic and necrotic cells were determined using annexin V-FITC/PI staining with flow cytometry. Data are shown as the mean  $\pm$  SD (n = 3). \* P < 0.05 versus non-treated control.

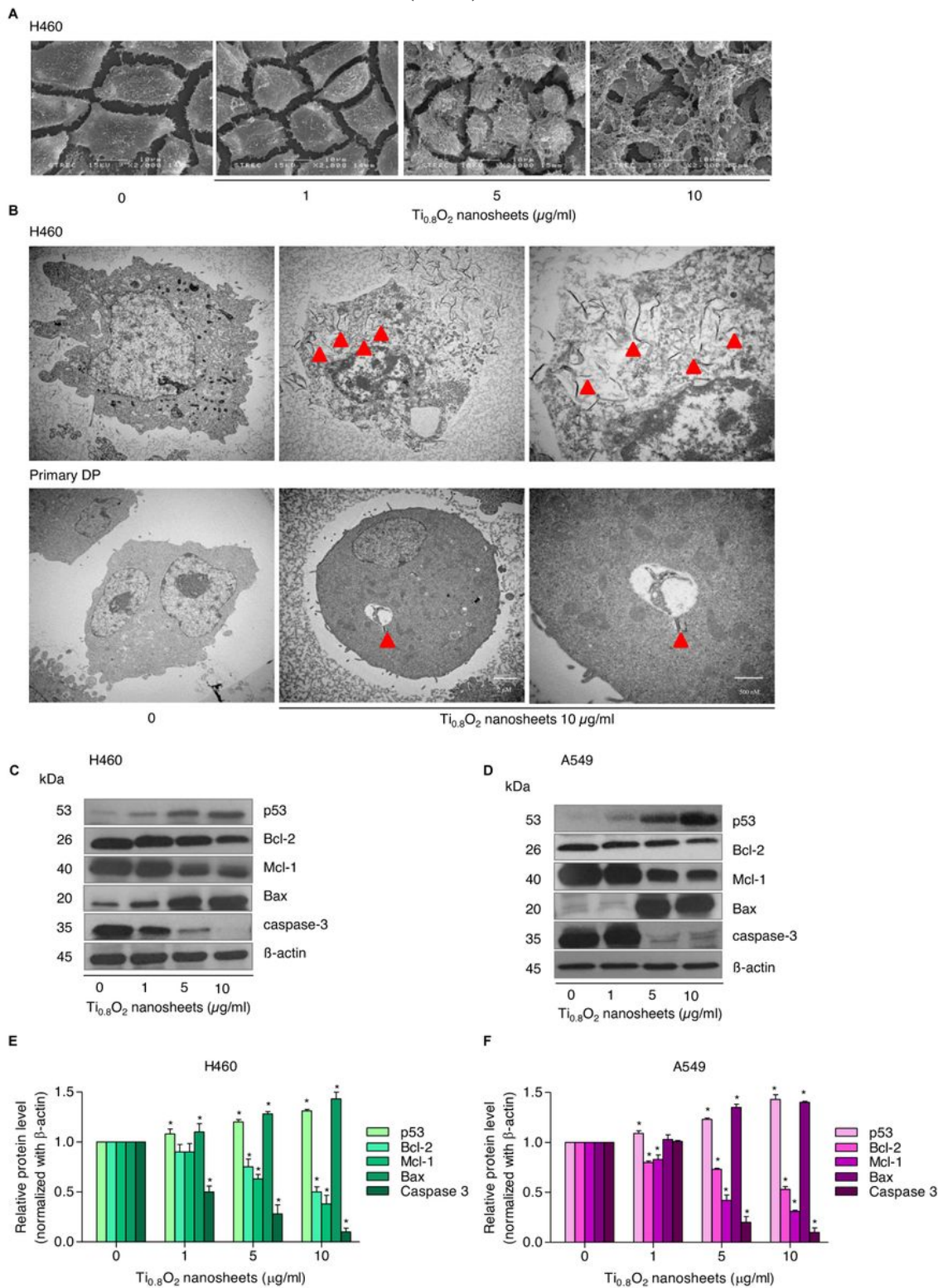


**Figure 3**

Morphology and characterization of cells when treated with Ti<sub>0.8</sub>O<sub>2</sub> nanosheets. A Morphology of H460 cells determined by scanning electron microscopy (SEM). B Cellular uptake of Ti<sub>0.8</sub>O<sub>2</sub> nanosheets in

H460 and primary DP cells at 24 h determined by transmission electron microscopy (TEM). C, D Effect of TiO<sub>2</sub>O<sub>2</sub> nanosheets on apoptosis-related proteins measured by Western blot analysis. Blots were reprobated with β-actin to confirm the equal loading of samples. E, F Relative protein levels calculated by densitometry. Data are shown as the mean ± SD (n = 3). \* P < 0.05 versus non-treated control

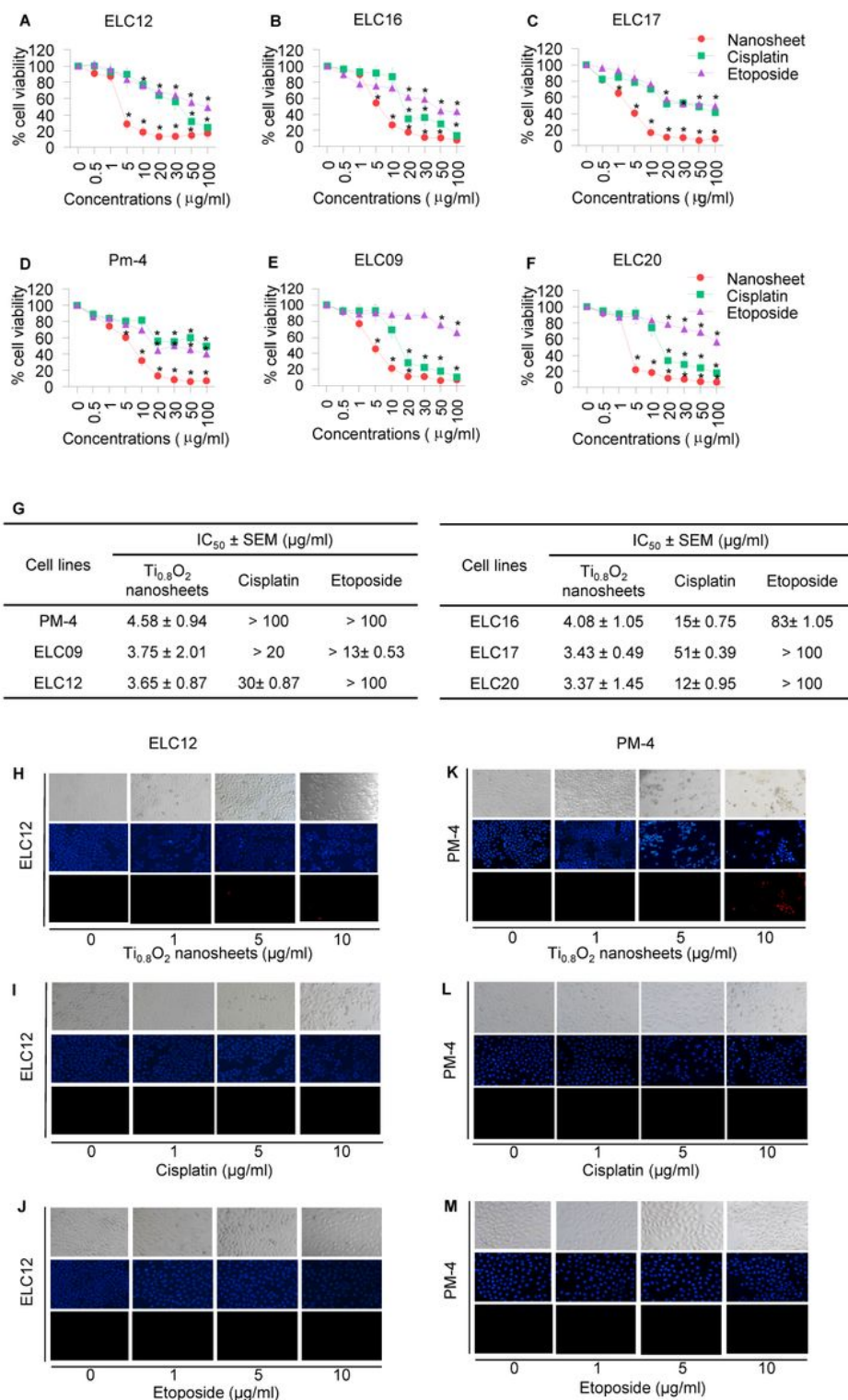
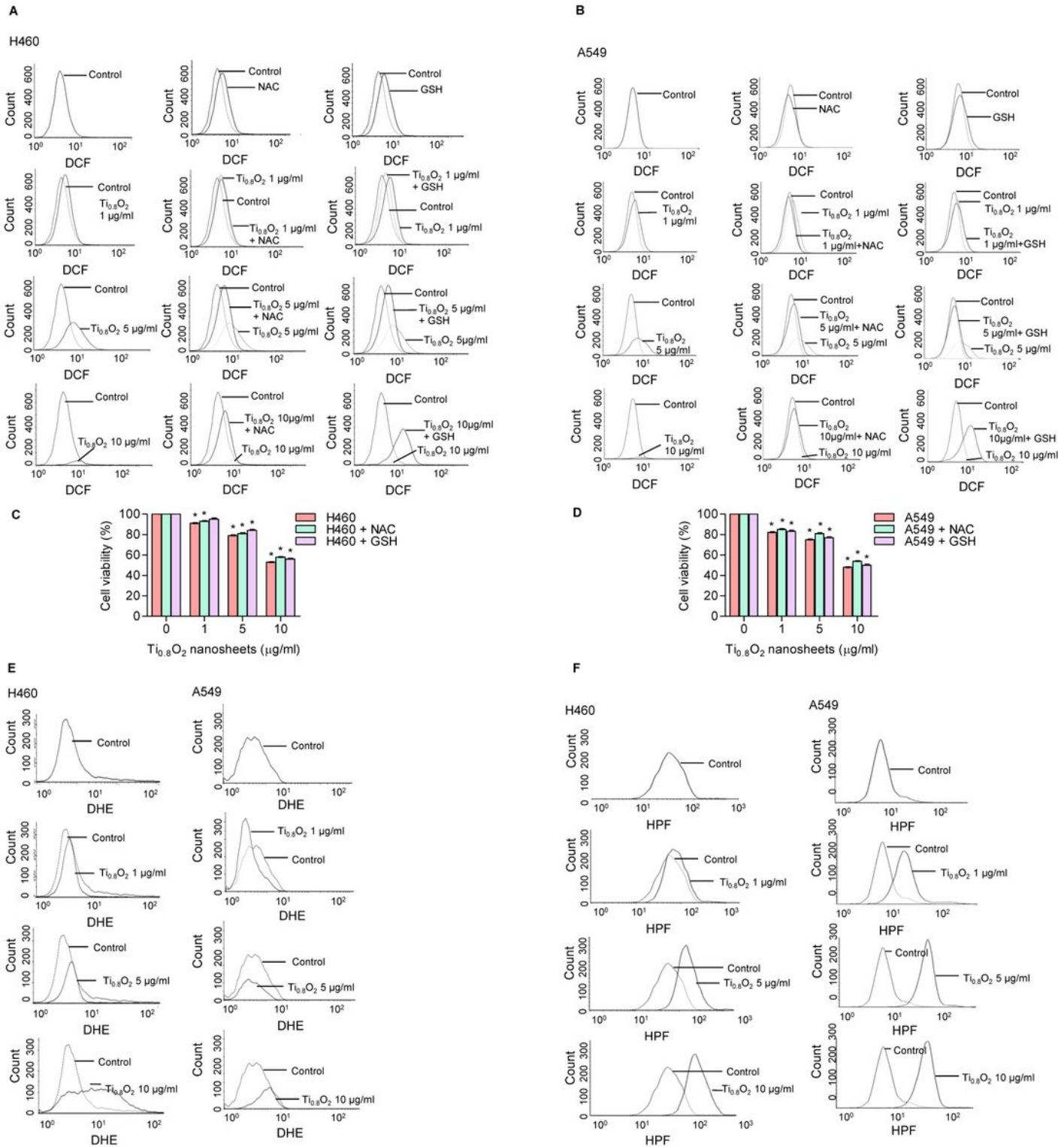


Figure 4

Cytotoxicity of the TiO<sub>2</sub> nanosheets on malignant pleural effusion from advanced lung cancer patients. A-F Effect of the TiO<sub>2</sub> nanosheets on the cell viability of malignant pleural effusion for 24 h using the MTT assay to determine the IC<sub>50</sub> values. G Percentages of cell viability were determined using the MTT assay. H-M Morphology of apoptotic nuclei stained with Hoechst 33342 dye and propidium iodide in cells treated with TiO<sub>2</sub> nanosheets, cisplatin and etoposide were determined by visualization under a fluorescence microscope; the percentages of nuclear fragments and PI positive cells were calculated. Data are shown as the mean ± SD (n = 3). \* P < 0.05 versus non-treated control



## Figure 5

TiO<sub>2</sub> nanosheets induced intracellular ROS in H460 and A549 cells. A, B The effect of TiO<sub>2</sub> nanosheets (0–10 µg/mL) on intracellular ROS induction at 24 h in H460 and A549 cells was determined by flow cytometry with the fluorescent probe DCF (10 µM). Cells were treated with TiO<sub>2</sub> nanosheets (0–10 µg/mL) alone for 24 h or with the pretreatment of 2.5 mM NAC and 2.5 mM GSH. C, D Effect of TiO<sub>2</sub> nanosheets on cell viability in H460 and A549 cells at 24 h with the pretreatment of 2.5 mM NAC or 2.5 mM GSH was determined by the MTT assay. Data are shown as the mean ± SD (n = 3). E The effect of TiO<sub>2</sub> nanosheets (0–10 µg/mL) on superoxide anion induction at 24 h in H460 and A549 cells was determined by flow cytometry with the fluorescent probe DHE (10 µM). F The effect of TiO<sub>2</sub> nanosheets (0–10 µg/mL) on hydroxyl radical induction at 24 h in H460 and A549 cells was determined by flow cytometry with the fluorescent probe HPF (10 µM).

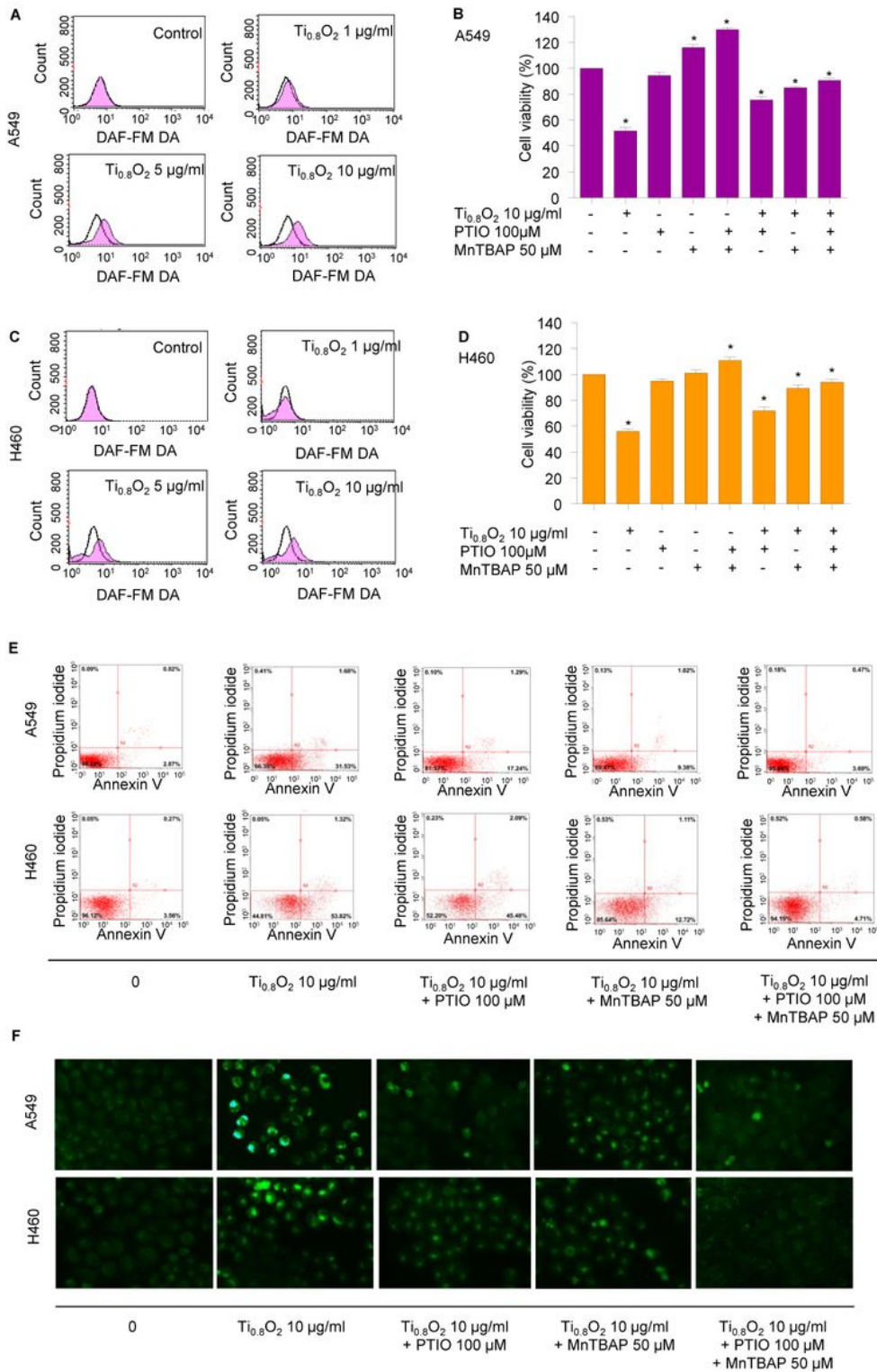


**Figure 6**

Ti<sub>0.8</sub>O<sub>2</sub> nanosheets induced NO in A549 and H460 cells and mediated peroxynitrite generation in these cells. A, C Effect of Ti<sub>0.8</sub>O<sub>2</sub> nanosheets on NO levels in A549 and H460 cells. Cells were treated with DAF-FM DA and various concentrations of Ti<sub>0.8</sub>O<sub>2</sub> nanosheets (0–10 µg/mL) for 30 min and the peroxynitrite levels were determined at 3 h by flow cytometry. B, D The cytotoxic effect of Ti<sub>0.8</sub>O<sub>2</sub> nanosheets and NO scavenger (PTIO) on A549 and H460 cells. Effect of Ti<sub>0.8</sub>O<sub>2</sub> nanosheets and NO scavenger (PTIO) on cell

viability. Cells were treated with TiO<sub>2</sub> nanosheets (10 µg/mL) in the presence or absence of pretreatment with a NO scavenger (PTIO) (100 µM) or pretreatment with a superoxide inhibitor (MnTBAP) (50 µM) for 24 h by MTT assay. E Apoptotic and necrotic cells were determined using annexin V-FITC/PI staining with flow cytometry. F Cellular NO level stained with DAF-FM DA in cells treated with TiO<sub>2</sub> nanosheets (10 µg/mL) or pretreated with PTIO (100 µM) or pretreated with MnTBAP (50 µM) were determined by visualization under a fluorescence microscope.

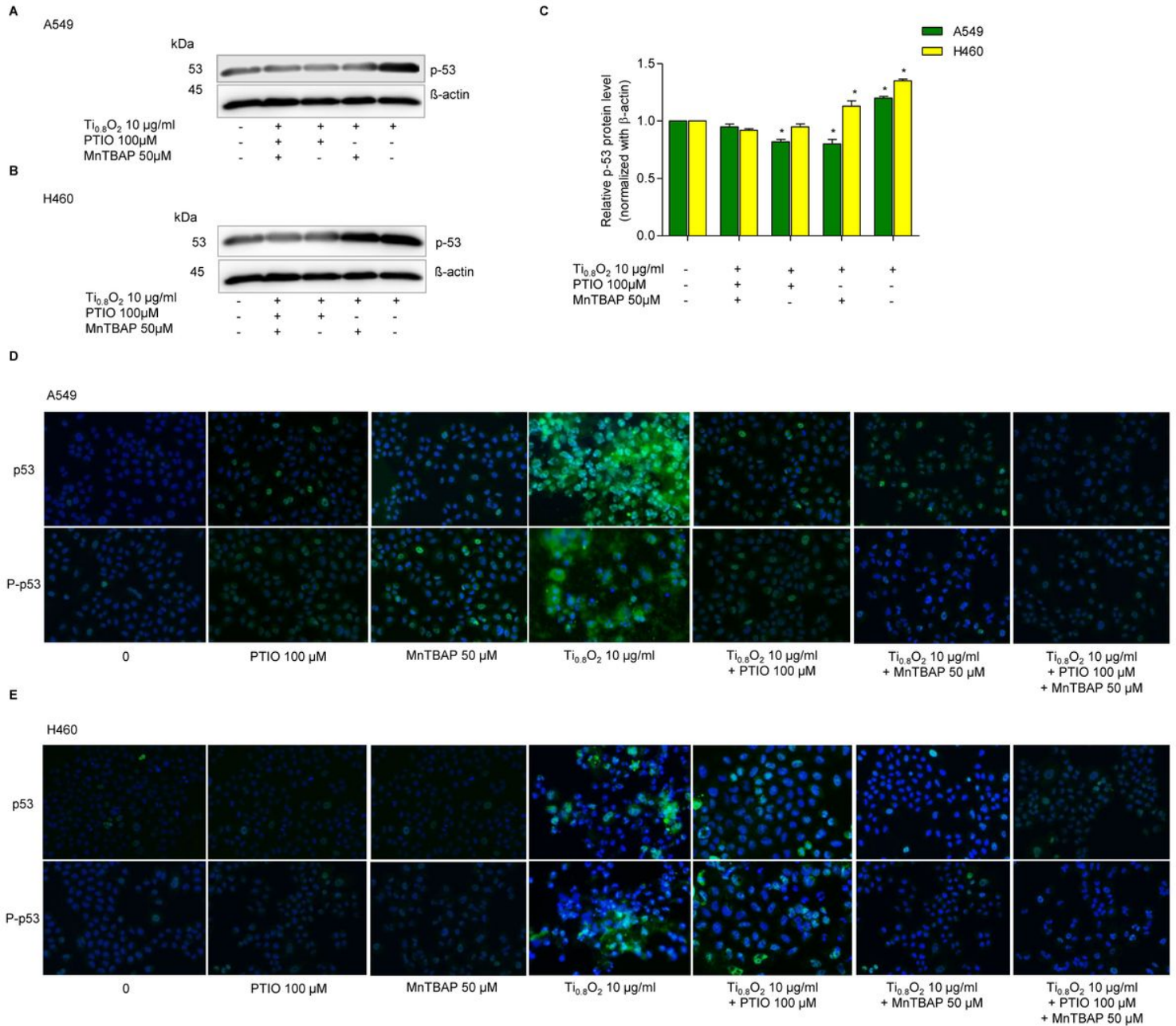


**Figure 7**

TiO<sub>2</sub> nanosheets associated with apoptosis in A549 and H460 cells via p53 upregulation. A, B Peroxynitrite-potentiated cell apoptosis through the p53 protein was measured by Western blot analysis. C Blots were reprobated with β-actin to confirm the equal loading of samples. The relative protein levels were calculated by densitometry. Data are shown as the mean ± SD (n = 3). \* P < 0.05 versus non-treated

control. D, E The expressions of p53 and P-p53 were analyzed by immunofluorescence staining in A549 and H460 cells.

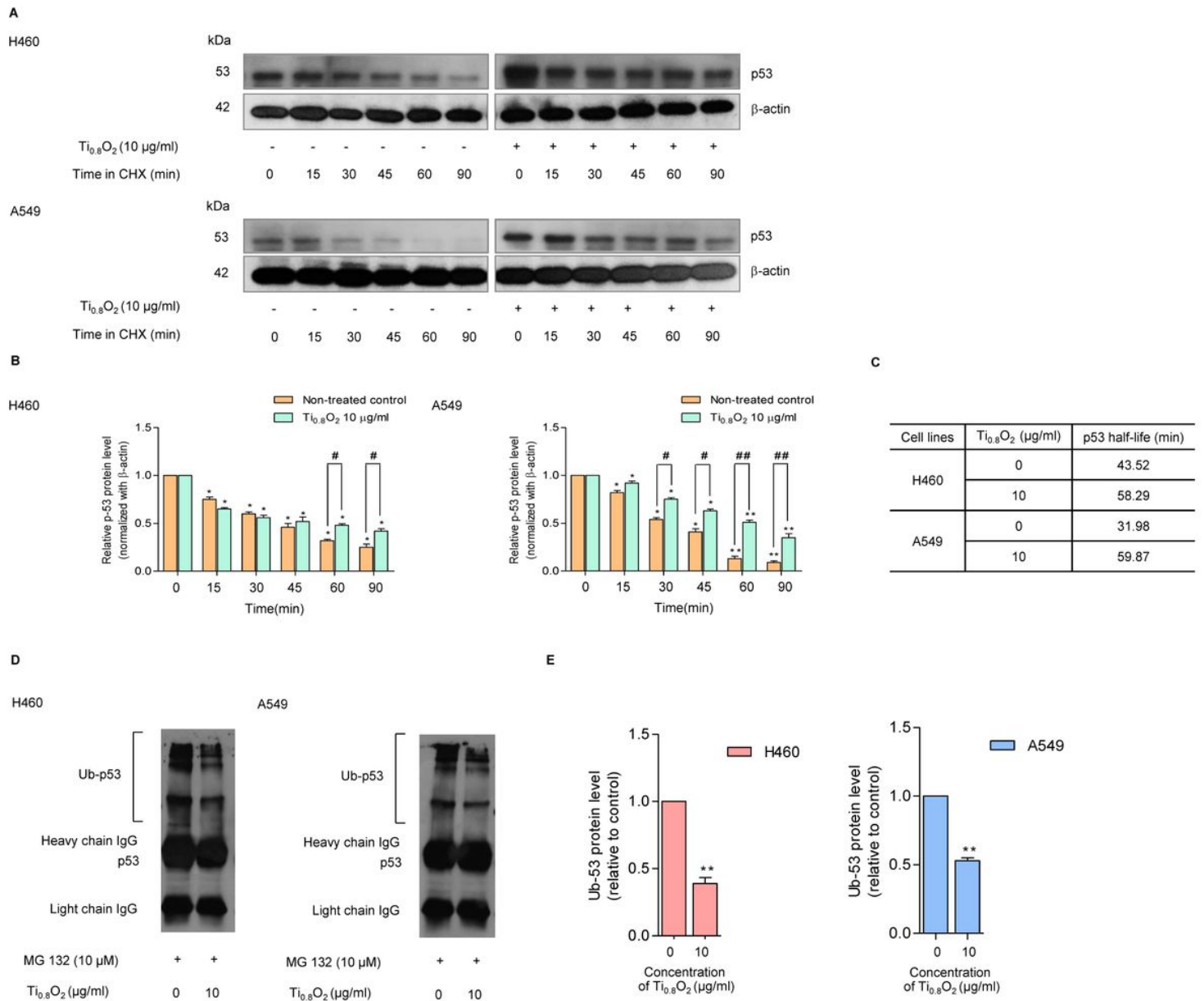


**Figure 8**

Ti<sub>0.8</sub>O<sub>2</sub> nanosheets increased p53 stability but not through the p53 proteasomal degradation. A The half-life of p53 was confirmed using the cycloheximide (CHX) chasing assay. H460 and A549 cell lines were treated with 50 µg/ml of CHX with or without 10 µg/ml Ti<sub>0.8</sub>O<sub>2</sub> nanosheets as indicated by the time in minutes. Western blot analysis was performed to evaluate the p53 protein level. B The relative p53 protein levels were calculated and compared with the non-treatment control at 0 min. C The half-lives of the p53 protein of H460 and A549 cells were calculated. D H460 and A549 cells were pretreated with 10 µM MG132 for 30 min followed by treatment with 10 µg/ml Ti<sub>0.8</sub>O<sub>2</sub> nanosheets for 60 min. The protein lysates were collected and incubated with a mixture of beads and p53 primary antibodies to pull out the protein of interest. Then, the ubiquitinated protein levels were measured by Western blot analysis. E Ub-

p53 levels were quantified by densitometry. The statistical calculation was compiled with repeated measured one-way ANOVA with Scheffé's post-hoc test for individual comparisons and the t-test for two group comparisons. The relative to control protein levels are reported. (n = 3) (\*p < 0.05, \*\*p < 0.01 compared with the untreated control at 0 min and # < 0.05, ## p < 0.01 compared with the untreated control at the same time).

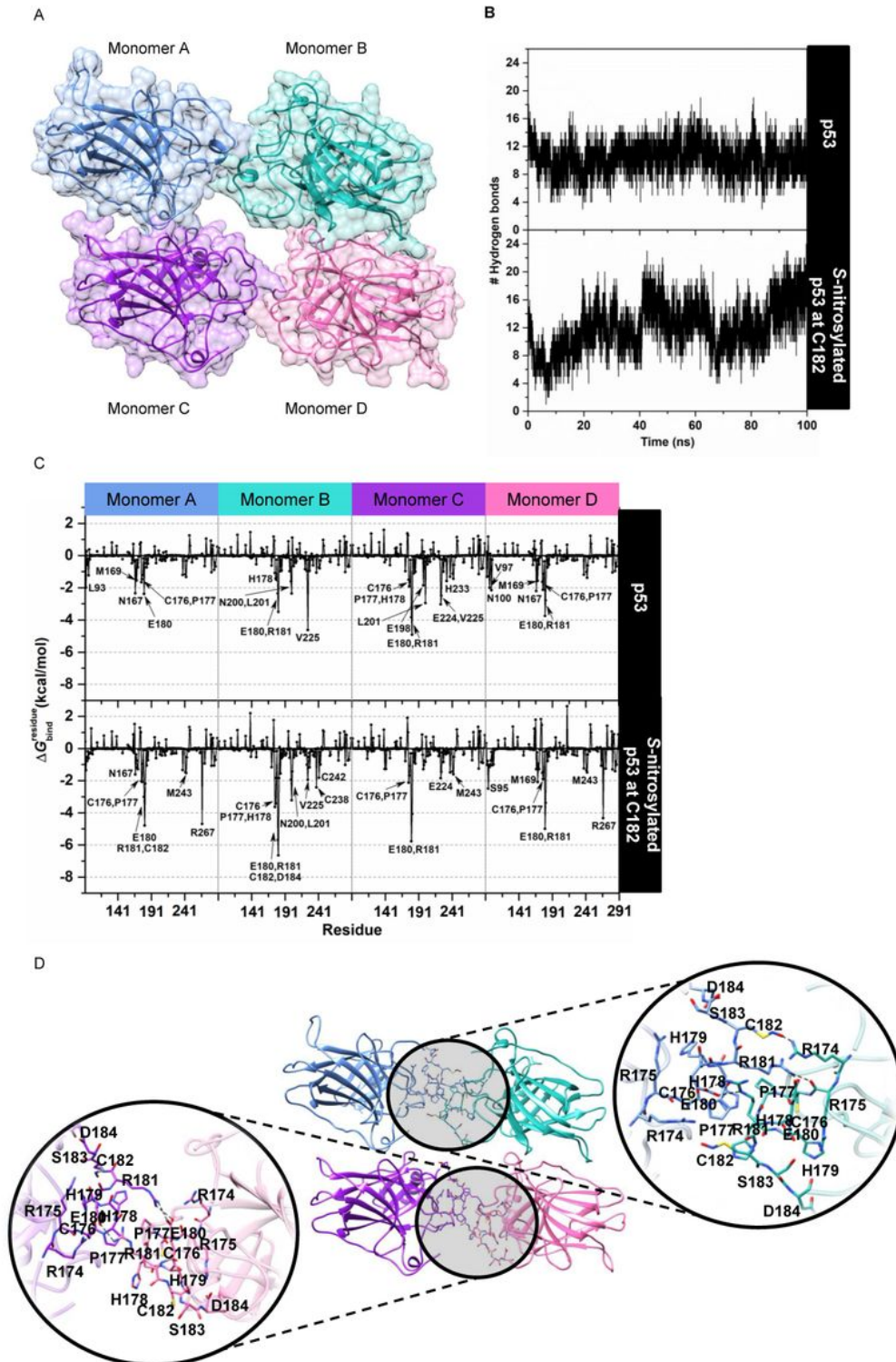


Figure 9

S-nitrosylation in the regulation of p53 stability. A Three-dimensional (3D) structure of the tetrameric p53 core domain without DNA bound (PDB ID: 3KMD). B Time evolution of the total number of intermolecular hydrogen bonds formed between each monomer of the p53 core domain and its adjacent monomer. C The plot of (kcal/mol) of the p53 tetramer for the native form (top) and the C182 S-nitrosylation (bottom) system. D The representative 3D structure taken from the last MD snapshot of the S-nitrosylation system, with hydrogen bonds and electrostatic interactions represented by black dashed lines.

## Supplementary Files

This is a list of supplementary files associated with this preprint. Click to download.

- [graphicalabstract.jpg](#)
- [SupplementaryMaterial.pdf](#)